Flat band based multifractality in the all-band-flat diamond chain

Aamna Ahmed[ID],[1] Ajith Ramachandran,[2] Ivan M. Khaymovich,[3] and Auditya Sharma[1]

[1]*Department of Physics, Indian Institute of Science Education and Research, Bhopal, Madhya Pradesh 462066, India*
[2]*Department of Physics, Christ College, Irinjalakuda, Kerala 680125, India*
[3]*Nordita, Stockholm University and KTH Royal Institute of Technology Hannes Alfvéns väg 12, SE-106 91 Stockholm, Sweden*

We study the effect of quasiperiodic Aubry-André disorder on the energy spectrum and eigenstates of a one-dimensional all-band-flat (ABF) diamond chain. The ABF diamond chain possesses three dispersionless flat bands with all the eigenstates compactly localized on two unit cells in the zero disorder limit. The fate of the compact localized states in the presence of the disorder depends on the symmetry of the applied potential. We consider two cases here: a symmetric one, where the same disorder is applied to the top and bottom sites of a unit cell and an antisymmetric one, where the disorder applied to the top and bottom sites are of equal magnitude but with opposite signs. Remarkably, the symmetrically perturbed lattice preserves compact localization, although the degeneracy is lifted. When the lattice is perturbed antisymmetrically, not only is the degeneracy is lifted but compact localization is also destroyed. Fascinatingly, all eigenstates exhibit a multifractal nature below a critical strength of the applied potential. A central band of eigenstates continue to display an extended yet nonergodic behavior for arbitrarily large strengths of the potential. All other eigenstates exhibit the familiar Anderson localization above the critical potential strength. We show how the antisymmetric disordered model can be mapped to a $\pi/4$ rotated square lattice with the nearest and selective next-nearest-neighbor hopping and a staggered magnetic field—such models have been shown to exhibit multifractality. Surprisingly, the antisymmetric disorder (with an even number of unit cells) preserves chiral symmetry—we show this by explicitly writing down the chiral operator.

I. INTRODUCTION

Highly degenerate dispersionless or *flat band* (FB) [1–5] systems, which support *compact localized eigenstates* (CLS) [6,7] have been of great interest over the last decade. The localization properties and associated repressed transport have been discussed in the context of engineered lattices in one, two, and three dimensions, such as diamond [8–10], cross-stitch [11–13], dice [14–17], honeycomb [18,19], kagome [20–22], and pyrochlore lattices [23,24]. The compact localized states have been experimentally found to exist in a range of setups such as Hubbard model systems [25,26], photonic systems [27,28], exciton-polariton condensates [20], and Bose-Einstein condensates [29].

In the most familiar type of localization, namely, Anderson localization [30,31], which is induced by on-site disorder, the "spread" of a state dies down exponentially with a well-defined notion of a characteristic localization length [32,33]. Compact localization, in contrast, is much stronger with the span restricted strictly to a few unit cells, with zero probability amplitude elsewhere. Paradoxically the interplay of both these types of strong localization results in a drop in localization. When a tiny amount of uniform disorder is turned on in a compactly localized all-band-flat (ABF) diamond chain, the eigenstates exhibit an extremely weak *flat band based localization* [34]. The disorder, in fact, facilitates the hybridization of the large-scale degenerate network of compact localized

eigenstates, and we see weak localization that is on the cusp of delocalization. In this work, we show that when the ABF chain is subjected instead to a quasiperiodic Aubry-André (*AA*) disorder [35,36], the eigenstates are in fact extended but nonergodic thus exhibiting multifractality, a delicate phenomenon that has attracted a wave of interest in recent times [37–55]. The familiar 1-D Aubry-André Harper (AAH) tight-binding model [48,56,57], which is endowed with self-duality [35,58] exhibits multifractality [31,59] only at the metal-insulator transition that occurs at a critical potential strength. Here, we report a robust *flat band based multifractality* (FBM) that is seen in an extensive region of the phase diagram.

Moreover, we find that the symmetry of the applied external potential is crucial [60–71]. A symmetric disorder, where the same disorder is applied to the top and bottom sites of a unit cell, causes a complete lift of degeneracy; however, remarkably we find that the CLS remain robust [72]. Although all the eigenstates are compactly localized over two unit cells, these cannot be obtained by translating the coefficients by an integer number of unit cells since the disorder breaks the translation symmetry. In contrast, when we apply the *AA* potential in an antisymmetric manner, where the disorder applied to the top and bottom sites of a unit cell are of equal magnitude but opposite sign, we find that both the degeneracy and compact localization are destroyed. A tiny disorder hybridizes the different compact localized states, resulting in flat band based multifractality. When the strength of the disorder is higher

than a critical value (where interband hybridization becomes possible), we recover conventional Anderson localization for all the eigenstates except those in a central band. Another of our striking findings is that when the lattice is perturbed antisymmetrically, the chiral symmetry of the Hamiltonian is left intact despite the presence of disorder. We show this with an explicit construction of the chiral symmetry operator that anticommutes with the Hamiltonian independent of the strength of the disorder.

The paper is organized as follows. In Sec. II, the ABF diamond chain, as well as the Aubry-André potential, are described. In Sec. III, we discuss the effects of applying the *AA* potential in the symmetric configuration that leaves the compact localization robust. In Sec. IV, we discuss the antisymmetric application of disorder, which supports multifractal states. In Sec. V, we present an analytic treatment in support of the numerical results discussed in Sec. IV. We then summarize our results in Sec. VI. The details of the lattice transformations used in Sec. V and numerical analysis of a variety of complementary quantities in support of the main findings are presented in Appendix.

II. MODEL

We consider the ABF diamond lattice [34], where each unit cell n consists of three sites labeled by u_n (up), c_n (center), and d_n (down), respectively. The corresponding single-particle states are conveniently represented in Dirac notation as $|u_n\rangle$, $|c_n\rangle$, and $|d_n\rangle$ respectively. The Hamiltonian is given by

$$\hat{H} = -J \sum_{n=1}^{N/3} (-|u_n\rangle\langle c_n| + |d_n\rangle\langle c_n| + |c_n\rangle\langle u_{n+1}|$$

$$+ |c_n\rangle\langle d_{n+1}| + \text{H.c.})$$

$$+ \sum_{n=1}^{N/3} (\zeta_n^u |u_n\rangle\langle u_n| + \zeta_n^c |c_n\rangle\langle c_n| + \zeta_n^d |d_n\rangle\langle d_n|). \quad (1)$$

Since each unit cell has three sites, the total number of sites denoted by N should be a multiple of 3. All the energy terms are represented in hopping amplitude J units, assuming $J = 1$ for simplicity. For each site of the nth unit cell, we include on-site energy using independent Aubry-André potentials

$$\zeta_n^\alpha = \lambda_\alpha \cos(2\pi n b + \theta_p), \quad (2)$$

where the strength of the potential is λ_α and α can take the values u, c and d. The quasiperiodicity parameter b must be an irrational number which we set to be the golden mean $(\sqrt{5} - 1)/2$. θ_p is an arbitrary global phase chosen randomly from a uniform distribution in the range $[0, 2\pi]$. Also, periodic boundary conditions have been assumed [73].

The ABF diamond chain is a particular case of the Hamiltonian for which the on-site energies ζ_n are zero. This system possesses three flat bands at energies ± 2 and 0 and no dispersive bands. Consequently, the system possesses only compact localized eigenstates. Hence, the system is highly degenerate and also a good insulator. The Hamiltonian in the zero-disorder limit possesses chiral symmetry [74–76], which is represented by a k-independent operator $\Gamma_0 = \text{diag}(1, 1, -1)$. This operator is unitary since $\Gamma_0^2 = \mathbb{I}$ and $\Gamma_0 \mathcal{H}^\dagger(k) \Gamma_0^{-1} =$
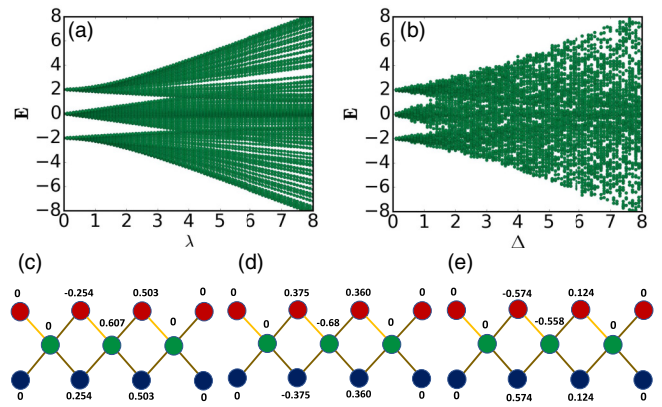
FIG. 1. The spectrum of the ABF diamond lattice in the symmetric case with (a) increasing strength of the quasiperiodic potential λ and (b) uniform uncorrelated random disorder with increasing strength Δ on the u and d sites. Schematic representations of the diamond chain: compact localized states from the (c) lower band ($E = -2.49$), (d) middle band ($E = -0.025$), and (e) upper band ($E = 2.51$) at $\lambda = 2$ (the amplitudes are obtained numerically). The system size is $N = 126$.

$-\mathcal{H}(k)$. Since the chiral operator Γ_0 anticommutes with the Hamiltonian, for each eigenvalue E with eigenvector $|\phi_E\rangle$ the negative $-E$ is also an eigenvalue with eigenvector $\Gamma_0 |\phi_E\rangle$.

In upcoming sections, we introduce the quasiperiodic Aubry-André potential on the ABF diamond chain, and investigate how it affects the spectrum and the compact localized states. Broadly there are two natural ways in which the on-site energies on the up and down sites may be correlated: a symmetric configuration in which $\zeta_n^u = \zeta_n^d$ and an antisymmetric configuration in which $\zeta_n^u = -\zeta_n^d$. Furthermore, we discuss two sub-cases within the symmetric setup: one in which the Aubry-André potential is applied on the u and d sites, and the second one in which the Aubry-André potential is applied on the c sites while keeping the u and d sites at zero potential.

III. SYMMETRIC APPLICATION OF AUBRY-ANDRÉ POTENTIAL

A. AA potential on the *u* and *d* sites

First, we consider the symmetric configuration:

$$\zeta_n^u = \zeta_n^d \quad \text{and} \quad \zeta_n^c = 0. \quad (3)$$

The introduction of the *AA* potential, i.e., $\zeta_n^u = \lambda \cos(2\pi n b + \theta_p)$ lifts the degeneracy of all the flat bands, as can be seen from Fig. 1(a). The eigenstates of the Hamiltonian are found to reside on two unit cells even in the presence of the *AA* potential [see Fig. 1(c)–1(e)]. Remarkably, the compactness of the eigenstates is preserved at higher strengths of the potential, even after all the bands mix and the system exhibits a single-band energy spectrum. Also, although the spectrum appears to be symmetric with respect to $E = 0$, a closer look reveals that this is not quite true. There is no requirement that every energy E comes with its negative counterpart $-E$ since the disorder breaks the chiral symmetry.

Interestingly, as shown in Fig. 1(b), when the applied potential is drawn from a uniform uncorrelated random dis-
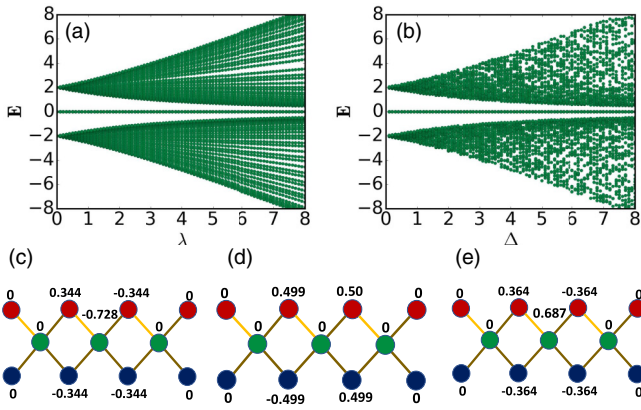
FIG. 2. The spectrum of the ABF diamond lattice with (a) *AA* potential with increasing quasiperiodic strength λ and (b) uniform uncorrelated random disorder with increasing strength Δ on the central *c* sites. Schematic representations of the diamond chain with the *AA* potential only on the *c* sites. CLSs for the (c) lower band ($E = -2.12$), (d) middle band ($E = 0$) (e) upper band ($E = 1.89$) at $\lambda = 5$. The system size is $N = 126$.

tribution $[-\Delta, \Delta]$, the results are similar (to those with quasiperiodic disorder of the same strength λ). We conclude that the presence of the compact localized states is a consequence of the symmetric application of the disorder and not the details of the applied potential. There exists a useful transformation to a new lattice (see Appendix A 1), which in the disorder-free limit, takes the system to a set of completely uncoupled sites. From Fig. 8(a), we observe that the transformation results in a lattice made of three-site unit cells but with an absence of intercell hopping, indicating the preservation of the CLSs (see Appendix A 2).

B. AA potential on the *c* sites

Next, we consider the case when disorder is introduced only on the *c* sites, i.e.,

$$\zeta_n^u = \zeta_n^d = 0 \quad \text{and} \quad \zeta_n^c \neq 0. \tag{4}$$

This is a special type of symmetric configuration. The energy spectrum with increasing strength of potential has been plotted for both the *AA* potential, i.e., $\zeta_n^c = \lambda \cos(2\pi nb + \theta_p)$ [see Fig. 2(a)] and for the uniform disorder case [see Fig. 2(b)], i.e., ζ_n^c drawn uniformly from $[-\Delta, \Delta]$. We observe that in both the cases, the degeneracies of the eigenstates are broken for the upper and lower bands, while the flatband at $E = 0$ remains robust even at higher disorder strengths. Further, the associated eigenstates preserve compact localization in both cases. We have numerically verified the same, as shown in the case of *AA* potential with $\lambda = 5$ in Figs. 2(c)–2(e). With the help of the transformation discussed in Appendix A 1, we show that the lattice is made of three-site unit cells but with an absence of intercell hopping, indicating the preservation of the CLSs [see Fig. 8(b)]. Additionally, each unit cell has a decoupled site which strengthens the observation of a robust flatband even in the presence of the disorder.

IV. ANTISYMMETRIC APPLICATION OF AUBRY-ANDRÉ POTENTIAL

As a further step, we consider the impact of the application of the *AA* potential in an antisymmetric manner, defined by

$$\zeta_n^u = -\zeta_n^d = \lambda \cos(2\pi nb + \theta_p) \quad \text{and} \quad \zeta_n^c = 0. \tag{5}$$

Here we observe that the introduction of the tinest of disorder results in the loss of compact localization of the energy eigenstates. Hence we explore the localization characteristics as a function of the disorder strength λ with the aid of several measures: inverse participation ratio (IPR), multifractal dimensions and level spacings.

The localization characteristics of the eigenstates can be understood with the help of the inverse participation ratio (IPR), which is defined as

$$I_2 = \sum_{n=1}^{\frac{N}{3}} \sum_{\alpha=u,c,d} |\psi_k(\alpha_n)|^4, \tag{6}$$

where the kth normalized single-particle eigenstate $|\psi_k\rangle = \sum_{n,\alpha} \psi_k(\alpha_n)|\alpha_n\rangle$ is written in terms of the Wannier basis $|\alpha_n\rangle$, representing the eigenstate of a single-particle localized at the site α ($\alpha = u, c, d$) in the nth unit cell of the lattice. For a completely localized eigenstate $I_2 = O(1)$ (when the state is localized on a few sites), while for a perfectly delocalized eigenstate $I_2 = O(1)/N$. Figure 3(a) shows the disorder-averaged IPR as a function of the strength of the antisymmetric *AA* potential for the entire spectrum. The detuned spectrum is confined within the limit $-2\lambda \leqslant E \leqslant 2\lambda$, with the bandwidth showing a roughly linear relation with λ. The introduction of the potential lifts the degeneracy of all the bands and also modifies the localization properties of the eigenstates. We observe that all the eigenstates for $\lambda \lesssim 1.5$ as well as those associated with the central band for any strength of the potential are extended while the remaining eigenstates show localization at higher strengths of the potential.

It turns out that the central band of extended eigenstates are well-described by a fractal mobility edge $|E| < 4/\lambda$ conjectured in a recent preprint [77]. Figure 3(b) shows the IPR averaged over the eigenstates separated by the fractal mobility edge $\lambda = 4/|E|$ [77]. The IPR of states constituting the inner section shows system-size dependence and is $\simeq 10^{-3}$, which is a signature of the extended nature of the eigenstates. However for the states comprising the outer section, IPR is independent of the system size and is close to unity, which is an indication of Anderson localization.

A. Multifractal analysis

We also analyze a quantity called the fractal dimension D_q [31,78,79] which is defined as

$$D_q = \frac{S_q}{\ln(N)}, \tag{7}$$

where N is the dimension of the Hilbert space and S_q are the participation entropies obtained from the kth eigenstate $|\psi_k\rangle = \sum_{n,\alpha} \psi_k(\alpha_n)|\alpha_n\rangle$ using the relation $S_q = \frac{1}{1-q} \ln I_q$,
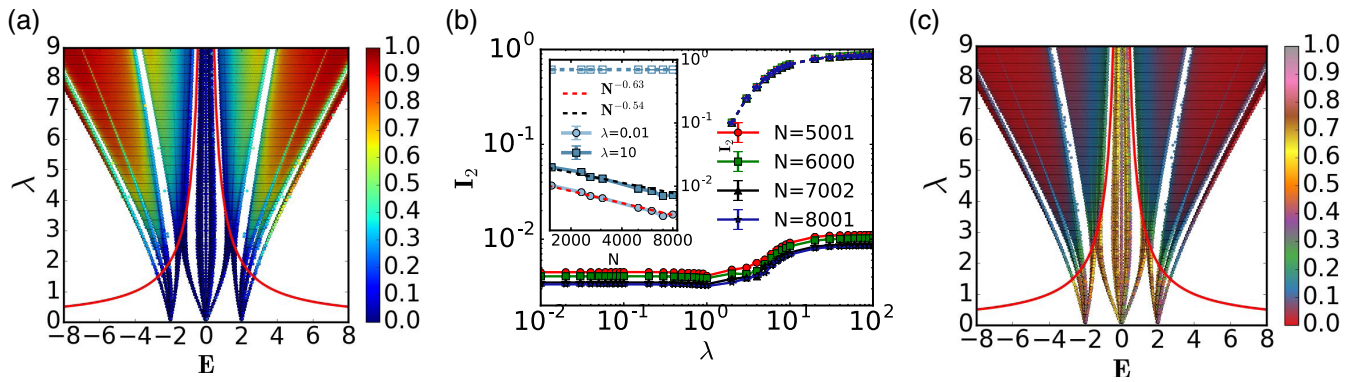
FIG. 3. I_2 and D_2 in the antisymmetric case. (a) The spectrum as a function of increasing strength λ, where the color denotes the value of I_2. The system size is $N = 6000$. (b) I_2 averaged over the eigenstates with increasing strength of *AA* potential λ for various system sizes averaged over 50 values of θ_p. Inset of (b) shows the scaling of $\langle I_2 \rangle$ with system size for $\lambda = 0.01$ and 10. Here the fitting for the multifractal states at $\lambda = 0.01$ ($\langle I_2 \rangle_{0.01} \sim N^{-0.63}$) is shown with red color and the fitting for the states at $\lambda = 10$ ($\langle I_2 \rangle_{10} \sim N^{-0.54}$) is shown with black color. (c) The spectrum as a function of increasing strength λ, where the color denotes the value of the fractal dimension D_2, defined in Eq. (7), for all the single-particle eigenstates. The system size is $N = 6000$. The red solid line in (a) and (c) given by $\lambda = 4/|E|$ shows the transition between multifractal and localized states, conjectured in Ref. [77] from the analogy to the extended Harper problem (see Sec. V for more details). In (b), I_2 averaged over the eigenstates drawn from the inner and outer regions separated by the fractal mobility edge are shown separately. Solid lines with filled symbols correspond to states in the inner region and dashed lines with open symbols to states in the outer region. We observe that the open symbols corresponding to different system sizes overlap indicating that these states are localized.

where

$$I_q = \sum_{n=1}^{\frac{N}{3}} \sum_{\alpha=u,c,d} |\psi_k(\alpha_n)|^{2q} \qquad (8)$$

are the qth order moments. While considering the ensemble average, the fractal dimension can be defined in two forms [80,81]; the first one uses arithmetically ensemble-averaged moments $\langle I_q \rangle$ after which the logarithm is taken:

$$\tilde{D}_q = \frac{1}{1-q} \frac{1}{\ln N} \ln \langle I_q \rangle. \qquad (9)$$

In the second approach, the averaging is done in a geometric fashion, i.e., after taking the logarithm:

$$D_q = \frac{1}{1-q} \frac{1}{\ln N} \langle \ln I_q \rangle. \qquad (10)$$

Also, $\tilde{D}_q$ is a lower bound to D_q from Jensen's inequality, i.e., $\tilde{D}_q \leqslant D_q$, since logarithm is a concave function. For $q = 2$, one obtains $S_2 = -\ln(I_2)$. Figure 3(c) shows D_2 as a function of the strength of the antisymmetric *AA* potential for the entire spectrum. We observe the presence of the fractal mobility edge conjectured recently [77] using an analogy to the extended Harper problem (see Sec V). The fractal mobility edge ($\lambda \leqslant 4/|E|$) is shown by the red curves in Fig. 3(c), separating the multifractal wave functions (extended but nonergodic) with $0 < D_2 < 1$, from the Anderson localized eigenstates (red color signifies $D_2 \approx 0$). Here we also study the scaling of IPR ($\langle I_2 \rangle$) with system size (see inset of Fig. 3(b)). The IPR scales as $N^{-\tilde{D}_2}$ [82]. We observe from the inset of Fig. 3(b) that for $\lambda = 0.01$, IPR scales as $N^{-0.63}$, which reaffirms the multifractal nature of the eigenstates at low potential strengths.

The fractal dimension in the limit $N \to \infty$ is given by [31]

$$D_q^\infty = \lim_{N \to \infty} D_q. \qquad (11)$$

For a perfectly delocalized state, $D_q^\infty = 1$ while for a localized state S_q is a constant, as observed for Anderson localization and results in vanishing D_q^∞ for all $q > 0$. For intermediate cases, $0 < D_q^\infty < 1$, which is a sign that the state is extended but nonergodic. Further, the eigenstates are multifractal if D_q^∞ depends nontrivially on $q > 0$ while for a constant $0 < D_q^\infty < 1$, the states are fractal. The q dependence of the fractal dimension D_q is shown in Fig. 4(a). We observe that for all $q > 0$, $0 < D_q < 1$ with a nontrivial dependence on the moment q. This indicates that all the eigenstates in the low-λ region exhibit multifractal nature.

For large enough N, the IPR is given by the expression

$$I_q = c_q N^{-D_q^\infty}, \qquad (12)$$

with a certain c_q, weakly dependent on N. This leads to the finite-size D_q being linear in $1/\ln N$ [see Fig. 4(b)] and allows one to extract D_q^∞ via a linear extrapolation in $1/\ln N$ [81]. We observe that in the limit of $N \to \infty$, the fractal dimension tends to a value significantly lower than unity. It can be concluded that the multifractality seen here is robust against increasing system sizes. Moreover, we have also verified that the system size dependence of D_q seen here is very similar to what is displayed by the AAH model at the critical point.

Another useful method to distinguish between localized, multifractal and delocalized phases is to carry out an analysis of the even-odd (odd-even) spacings of the energy eigenvalues E_k (arranged in ascending order) [49]. They are defined as $s_k^{e-o} = E_{2k} - E_{2k-1}$ and $s_k^{o-e} = E_{2k+1} - E_{2k}$ for even-odd and odd-even cases, respectively. For a localized state, the gap vanishes as both the spacings exhibit the same form. In the multifractal case, the distributions of both spacings are strongly scattered. We observe from Fig. 5(a) that at $\lambda = 0.01$, both the spacings are scattered for the entire energy spectrum, indicating that all the eigenstates are multifractal in the low potential regime. From Fig. 5(b), we observe that while there is strong scattering corresponding to the states at the center
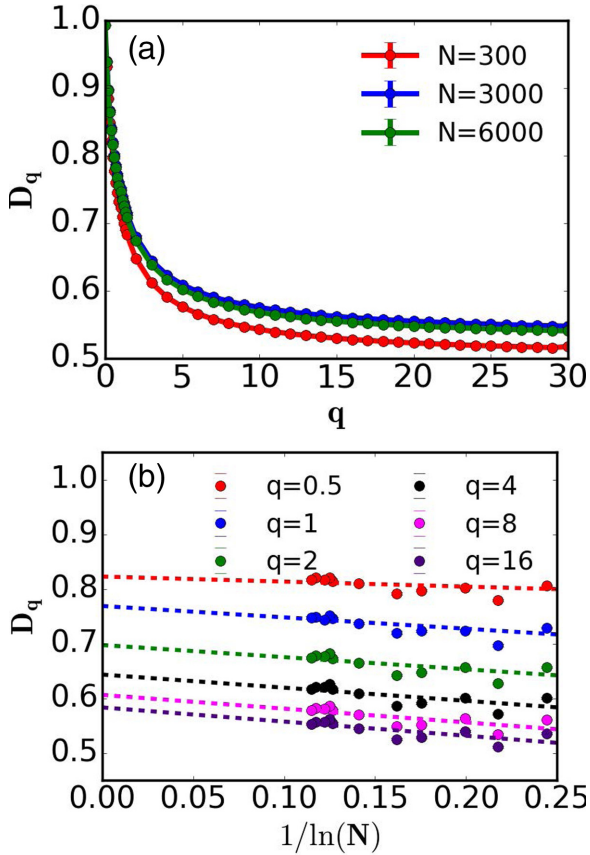
FIG. 4. In the antisymmetric case, (a) fractal dimension D_q vs q for various system sizes. (b) Fractal dimension D_q vs $\frac{1}{\ln(N)}$ for various q values and system sizes ranging from $N = 60$ to 6000. Here quasiperiodic strength $\lambda = 0.01$ and D_q is averaged over all the eigenstates for at least 50 values of θ_p.

($|E| < 4/\lambda$), the gap begins to vanish as one move toward the edges. At higher potential strengths, for example $\lambda = 100$ [see Fig. 5(c)], except for the level spacing at the center, the gap completely disappears, indicating localization.

It is well known that multifractal states are characterized by a broad distribution in energy gaps [83,84]. To study this aspect, we show plots of E_k and $s_k = E_{k+1} - E_k$ for various λ, in Figs. 5(d)–5(i). We observe that at low potential strength, i.e., $\lambda = 0.01$, the energy spectrum has a large number of subbands [see inset of Fig. 5(d)], and fluctuations are observed in the spacing of these gaps [see Fig. 5(g)]. We also observe that the level spacing distribution of all the eigenstates at $\lambda = 0.01$ follows an inverse power law [56], indicating that all the eigenstates are multifractal in the low potential regime. From Fig. 3(c), the transition point from the fully extended regime to the mixed one with the mobility edge, $|E| = 4/\lambda$, is is observed to be around $\lambda \simeq 1.5$. The magnitude of the gap between the energy levels becomes larger as one moves toward the edges [Fig. 5(e)], which is accompanied by a decrease in the magnitude of fluctuations in those gaps [see Fig. 5(h)]. At higher potential strengths, for example, $\lambda = 10$ [see Fig. 5(f)], the spectrum is completely pure pointlike, and all the eigenstates except those in the central band show reduced fluctuations, indicating localization [see Fig. 5(i)].

We conclude that the presence of the *AA* potential in the antisymmetric case transforms the CLSs into multifractal states at low potential strengths below a critical value (i.e., below $\lambda \simeq 1.5$, which is about the gap between the flat bands in the zero disorder limit). At higher potential strengths where the bands hybridize, we observe that all the eigenstates localize except those in the central part of the spectrum, which display multifractal nature.

B. Chiral symmetry

The addition of diagonal disorder in the ABF diamond lattice breaks translational invariance. One would also expect diagonal disorder to break the chiral symmetry [85–87] as observed in the symmetric case. However, remarkably in the antisymmetric case, when N is even, we observe pairs of eigenvalues $\pm E$, despite the on-site disorder. We infer that the chiral symmetry of the lattice is not broken. Indeed this is confirmed explicitly by the identification of the chiral operator Γ which is required to be a local operator [74]:

$$\Gamma = \gamma_1 \oplus -\gamma_2 \oplus \gamma_3 \cdots = \bigoplus_{i=1}^{n} (-1)^{i-1}\gamma_i, \qquad (13)$$

where each of the matrices $\gamma_i = \begin{pmatrix} 0 & 1 & 0 \\ 1 & 0 & 0 \\ 0 & 0 & 1 \end{pmatrix}_i$ acts on the ith unit cell and n is the total number of unit cells. We can verify that $\Gamma^{-1}H^{\dagger}\Gamma = -H$, and that Γ is involutory since $\Gamma\Gamma^{\dagger} = \mathbb{I}$. When periodic boundary conditions are imposed, the chiral symmetry is valid only for an even number of unit cells.

Before we conclude, we remark that multifractal states have been reported to exist in systems with chiral symmetry. For the Anderson model in 2D [88] and 3D [89], chiral symmetry is known to induce multifractal states near the band center, the origin of which can be traced back to the power-law decay of the eigenstates. It has been observed that chiral symmetry tends to delocalize eigenstates close to the origin [90]. In 1D [91], it has been proved that eigenstates at the band center are not localized exponentially. Chiral symmetry combined with strong disorder induces power-law localization and multifractal states near the origin [89].

V. MULTIFRACTALITY IN ANTISYMMETRIC CASE: ANALYTICAL TREATMENT

In this section, we analytically uncover the origin of the multifractality in the antisymmetric case. The diamond lattice in the disorder-free limit can be described through matrices V and T which capture the intra-cell and intercell information respectively:

$$V = \begin{pmatrix} 0 & 0 & -1 \\ 0 & 0 & 1 \\ -1 & 1 & 0 \end{pmatrix}, \quad T = \begin{pmatrix} 0 & 0 & 0 \\ 0 & 0 & 0 \\ 1 & 1 & 0 \end{pmatrix}. \qquad (14)$$

For the on-site disorder, we introduce another matrix W_n given by

$$W_n = \begin{pmatrix} \zeta_n^u & 0 & 0 \\ 0 & \zeta_n^d & 0 \\ 0 & 0 & \zeta_n^c \end{pmatrix}. \qquad (15)$$
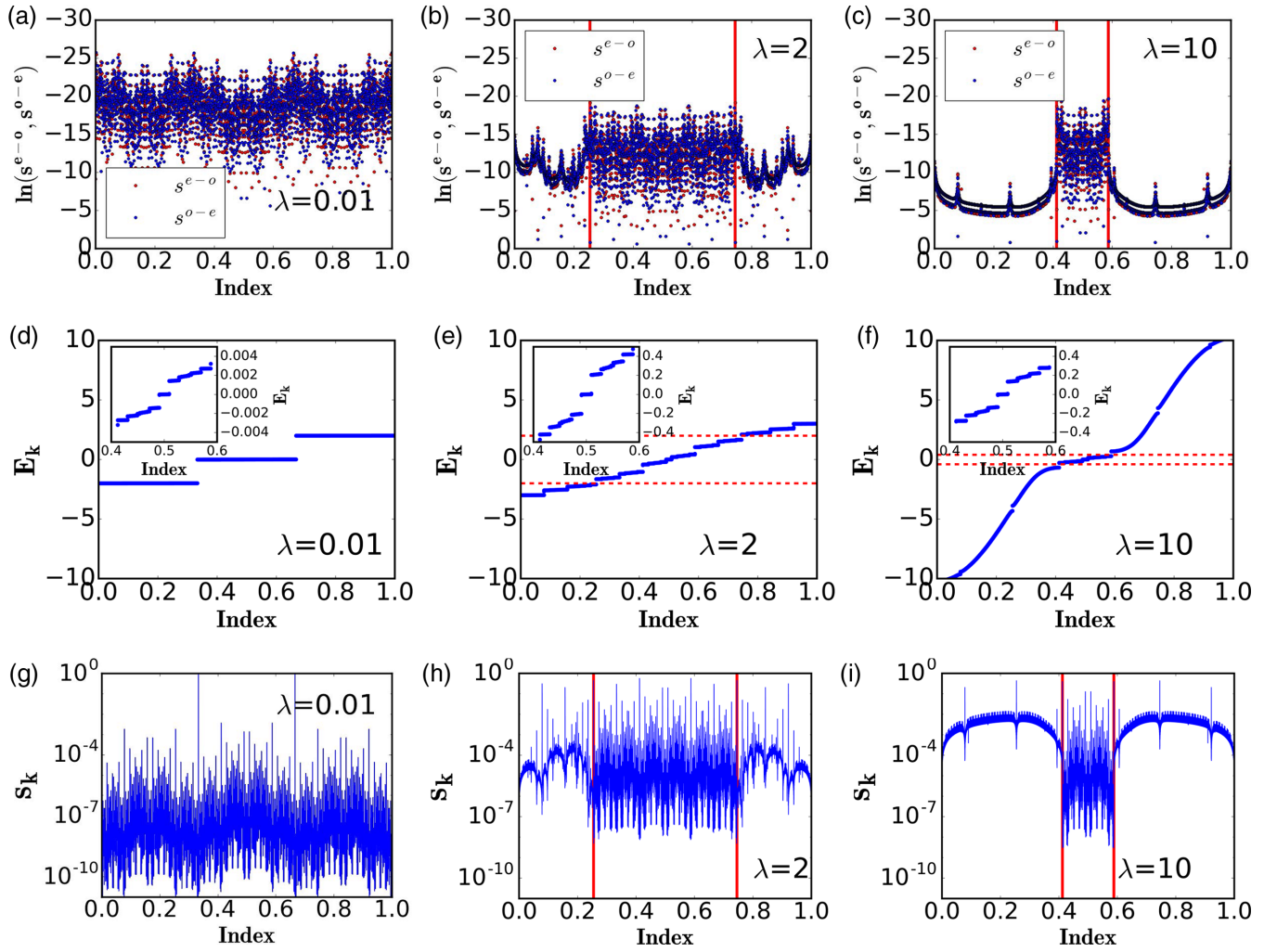
FIG. 5. In the antisymmetric case, (a)–(c) level spacing s_k^{e-o} (red) and s_k^{o-e} (blue) at quasiperiodic strength $\lambda = 0.01, 2$ and 10 respectively with averaging done over 50 values of θ_p. [(d)–(f)] Single-particle energy spectra E_k for $\lambda = 0.01, 2$, and 10, respectively. Inset shows the broken degeneracy for the states in the central band and (g)–(i) are corresponding level spacing s_k. Here index is the serial number of energy (gap) levels divided by the total number of gaps, and system size is $N = 6000$. For $\lambda = 2$ and 10, the indices corresponding to the fractal mobility edges $|E| = 4/\lambda$, are determined from (e)–(f). We have plotted them in the corresponding (b)–(c) and (h)–(i) using the vertical red lines.

The unitary matrix

$$U_1 = \frac{1}{\sqrt{2}} \begin{pmatrix} \frac{1}{\sqrt{2}} & -\frac{1}{\sqrt{2}} & 1 \\ -\frac{1}{\sqrt{2}} & \frac{1}{\sqrt{2}} & 1 \\ 1 & 1 & 0 \end{pmatrix}, \quad (16)$$

diagonalizes the V matrix when we carry out the transformation $V_1 = U_1 V U_1^\dagger$. The same transformation can be applied to the T matrix to obtain $T_1 = U_1 T U_1^\dagger$. The transformed matrices are

$$V_1 = \begin{pmatrix} -\sqrt{2} & 0 & 0 \\ 0 & \sqrt{2} & 0 \\ 0 & 0 & 0 \end{pmatrix}, \quad T_1 = \begin{pmatrix} 0 & 0 & 1 \\ 0 & 0 & 1 \\ 0 & 0 & 0 \end{pmatrix}. \quad (17)$$

Applying the same transformation on the matrix W_n, we obtain $(W_1)_n$ given by $U_1 W_n U_1^\dagger$:

$$(W_1)_n = \begin{pmatrix} \frac{\zeta_n^u}{4} + \frac{\zeta_n^d}{4} + \frac{\zeta_n^c}{2} & \frac{-\zeta_n^u}{4} + \frac{-\zeta_n^d}{4} + \frac{\zeta_n^c}{2} & \frac{\zeta_n^u}{2\sqrt{2}} - \frac{\zeta_n^d}{2\sqrt{2}} \\ \frac{-\zeta_n^u}{4} + \frac{-\zeta_n^d}{4} + \frac{\zeta_n^c}{2} & \frac{\zeta_n^u}{4} + \frac{\zeta_n^d}{4} + \frac{\zeta_n^c}{2} & \frac{-\zeta_n^u}{2\sqrt{2}} + \frac{\zeta_n^d}{2\sqrt{2}} \\ \frac{\zeta_n^u}{2\sqrt{2}} - \frac{\zeta_n^d}{2\sqrt{2}} & \frac{-\zeta_n^u}{2\sqrt{2}} + \frac{\zeta_n^d}{2\sqrt{2}} & \frac{\zeta_n^u}{2} + \frac{\zeta_n^d}{2} \end{pmatrix}. \quad (18)$$

In the antisymmetric case, $\zeta_n^c = 0$, $\zeta_n^u = -\zeta_n^d = \zeta_n$, yielding a simplification:

$$(W_1)_n = \frac{\zeta_n}{\sqrt{2}} \begin{pmatrix} 0 & 0 & 1 \\ 0 & 0 & -1 \\ 1 & -1 & 0 \end{pmatrix}. \quad (19)$$

The above transformation is a part of a series of lattice transformations shown in Appendix A 1. Using the lattice

equation:

$$(W_1)_n \psi_n - V_1 \psi_n - T_1 \psi_{n+1} - T_1^\dagger \psi_{n-1} = E \psi_n, \qquad (20)$$

the corresponding equation for the components $\psi_n = (u_n, d_n, c_n)^T$ can be written as

$$E u_n = \frac{\zeta_n}{\sqrt{2}} c_n - (-\sqrt{2} u_n + c_{n+1}), \qquad (21)$$

$$E d_n = -\frac{\zeta_n}{\sqrt{2}} c_n - (\sqrt{2} d_n + c_{n+1}), \qquad (22)$$

$$E c_n = \frac{\zeta_n}{\sqrt{2}} (u_n - d_n) - (u_{n-1} + d_{n-1}). \qquad (23)$$

Substituting u_n and d_n into Eq. (23), we get

$$E[E^2 - 4]c_n = \zeta_n^2 E c_n - 2\zeta_n c_{n+1} - 2\zeta_{n-1} c_{n-1}. \qquad (24)$$

Substituting $\zeta_n = \lambda \cos(2\pi n b + \theta)$, we have

$$\frac{2}{\lambda^2}\left[E^2 - 4 - \frac{\lambda^2}{2}\right] c_n = \cos(4\pi n b + 2\theta)c_n$$

$$- \frac{4}{\lambda E}[\lambda \cos(2\pi n b + \theta)c_{n+1}$$

$$+ \lambda \cos(2\pi (n-1) b + \theta)c_{n-1}]. \qquad (25)$$

The above equation resembles the extended Harper model [92], but with a doubled frequency of the on-site potential. Following the recent preprint [77], we compare the hopping amplitude $4/(\lambda|E|)$ with the level spacing amplitude $\max_n[\cos(4\pi n b + 2\theta) - \cos(4\pi (n+1) b + 2\theta)] \simeq 2 \sin(2\pi b)$ and conjecture that the transition between nonergodic extended and localized states should be at [93]

$$\lambda_c = \frac{4}{|E|}. \qquad (26)$$

An alternative way to see the emergence of multifractality in this model is provided by Thouless in his consideration of the Harper model [58,94]. Indeed, by taking the discrete Fourier transform:

$$c_{m,n} = \frac{1}{\sqrt{N}} \sum_k c_{n(\theta = \frac{2\pi k}{N} + \pi b)} e^{\frac{2\pi i}{N} km}, \qquad (27)$$

we get a 2D model without on-site potential, but with an effective magnetic flux, penetrating some of the plaquettes:

$$E\left[E^2 - 4 - \frac{\lambda^2}{2}\right] c_{n,m}$$

$$= \frac{E\lambda^2}{4}\left(e^{4i\pi b(n+\frac{1}{2})} c_{n,m+2} + e^{-4i\pi b(n+\frac{1}{2})} c_{n,m-2}\right)$$

$$- \lambda\left(e^{2i\pi b(n+\frac{1}{2})} c_{n+1,m+1} + e^{-2i\pi b(n+\frac{1}{2})} c_{n+1,m-1}\right)$$

$$- \lambda\left(e^{2i\pi b(n-\frac{1}{2})} c_{n-1,m+1} + e^{-2i\pi b(n-\frac{1}{2})} c_{n-1,m-1}\right), \qquad (28)$$

which is the $\pi/4$ rotated square lattice with nearest-neighbor and selected next-nearest-neighbor hoppings and a staggered magnetic field (see Fig. 6). Such models are also known to host multifractal states in an extended region of parameter space [95–97].

While our manuscript was under review, we came across a preprint [77] where the effect of quasiperiodic perturbations on one-dimensional all-band-flat lattice models has
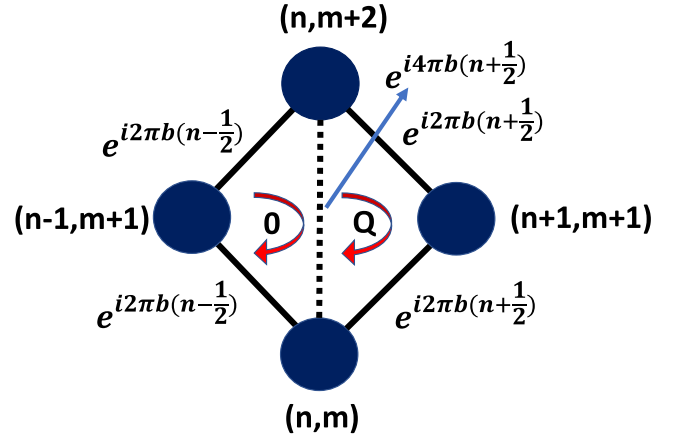
FIG. 6. A unit cell of the $\pi/4$ rotated square lattice with nearest-neighbor and selected next-nearest-neighbor hopping and staggered magnetic field showing the phases of the hopping on each link. The alternating fluxes 0 and $Q = 4\pi b$ are derived by summing the phases in the clockwise direction over each separate loop.

been investigated. There the authors discuss the presence of an energy-dependent critical-to-insulating transition where "fractality edges" separate localized states from critical states. In the case of the ABF diamond lattice with an antisymmetric application of disorder, they observed a critical-to-insulating transition at $|E| = 4/\lambda$. In the current version, we have confirmed the above conjecture with the aid of our numerical data as well as by a mapping of the Hamiltonian to other models known to host multifractal states from the literature before. Further, the substitution of $E = 0$ in Eq. (25) gives

$$0 = -2\lambda \cos(2\pi n b + \theta)c_{n+1} - 2\lambda \cos(2\pi (n-1) b + \theta)c_{n-1}. \qquad (29)$$

This model is equivalent to the off-diagonal Harper model [94,98] where the zero energy modes remain critical at all disorder strengths.

VI. CONCLUSION

This paper explores the effects of a quasiperiodic AA potential on a one-dimensional ABF diamond lattice. We find that the fate of the compact localized states is strongly dependent on the manner in which the potential is applied. We discuss the consequences when the potential is applied in two specific ways: symmetric and antisymmetric. When the diagonal disorder is applied symmetrically, the chiral symmetry of the lattice is broken. Although the large-scale degeneracy is destroyed, all the eigenstates remain compactly localized. It is also observed that the compact localization is independent of the precise nature of the applied perturbation, as long as it is applied in a symmetric manner. The inclusion of the potential only on the c sites is a particular case where CLSs are observed and the degeneracy of the central flat band is preserved.

In the antisymmetric case, the tiniest perturbation lifts the degeneracy, and the eigenstates no longer remain compactly localized. An exploration of the nature of the eigenvalues

and eigenfunctions through various observables shows the appearance of flatband-based multifractal states. Here all the wave functions are extended but nonergodic in the low disorder regime. All the bands start to hybridize at a critical potential strength, leading to conventional Anderson localization at higher magnitudes of λ. However, a central band is observed whose states continue to display extended behavior at all strengths of λ. A systematic study of the spectrum and the spacing between consecutive energy values is performed and compared with the AAH model. The robust existence of multifractal states with increasing disorder strength is a remarkable finding. Another interesting finding is that the chiral symmetry of the Hamiltonian is preserved in the presence of antisymmetric disorder when the total number of unit cells is even. In support of this finding, we are able to write down explicitly the chiral operator Γ.

The diamond lattice model in the zero-disorder limit can be converted through a series of transformations into a new lattice with decoupled sites. We study the effect of the same set of transformations for the diamond lattice model in the presence of disorder. We find that in the symmetric case, these transformations yield a lattice which displays an absence of intercell hopping, indicating the preservation of compact localization. On the other hand, the antisymmetric configuration of disorder supports the loss of CLSs owing to intercell hopping in the transformed lattice. Further, we demonstrate that our lattice transformations convert our Hamiltonian (with antisymmetric disorder) into a close relative of the extended Harper model and into a $\pi/4$ rotated square lattice with the nearest-neighbor and selective next-nearest-neighbor hopping and staggered magnetic field, both of which support the multifractality observed in the antisymmetric case.

We have seen that the introduction of the *AA* potential in a flat-band diamond chain yields interesting results within a single-particle setup. An exciting direction for research would be to explore the physics of such systems in the presence of interactions, and in particular, to look for flat band based *many-body* localization phenomena. We also look forward to future studies that can extend these ideas to two and three dimensional systems.

APPENDIX A: LATTICE TRANSFORMATION

In this section, a series of transformations are presented, whose application to the Hamiltonian of the diamond chain gives a new lattice which has decoupled sites in the zero-disorder limit. We utilize a similarity transformation to obtain a new Hamiltonian whose spacial arrangement of the sites significantly differs from the original lattice following the work of Danieli *et al.* [99]. On the one hand, this process identifies new flat band lattices and, on the other hand, helps in understanding the influence of the symmetry of the applied potential. We first present the transformation of the unperturbed ABF diamond chain. We then discuss the effect of the symmetric and antisymmetric configuration of disorder on the ABF diamond chain with the help of these transformations.

1. Transformation of unperturbed ABF diamond chain

The unperturbed diamond chain shown in Fig. 7(a) consists of three sites per unit cell. The intracell and intercell information of the Hamiltonian can be represented by V and T respectively and is given by

$$V = \begin{pmatrix} 0 & 0 & -1 \\ 0 & 0 & 1 \\ -1 & 1 & 0 \end{pmatrix}, \quad T = \begin{pmatrix} 0 & 0 & 0 \\ 0 & 0 & 0 \\ 1 & 1 & 0 \end{pmatrix}. \quad \text{(A1)}$$

Thus the lattice equation is

$$-V\psi_n - T\psi_{n+1} - T^\dagger \psi_{n-1} = E\psi_n, \quad \text{(A2)}$$

with $\psi_n = (u_n, d_n, c_n)^T$ being the tight binding representation of the wave function for the nth unit cell. Considering the unitary matrix

$$U_1 = \frac{1}{\sqrt{2}} \begin{pmatrix} \frac{1}{\sqrt{2}} & -\frac{1}{\sqrt{2}} & 1 \\ -\frac{1}{\sqrt{2}} & \frac{1}{\sqrt{2}} & 1 \\ 1 & 1 & 0 \end{pmatrix}, \quad \text{(A3)}$$

we perform the transformations $V_1 = U_1 V U_1^\dagger$ and $T_1 = U_1 T U_1^\dagger$ yielding new matrices

$$V_1 = \begin{pmatrix} -\sqrt{2} & 0 & 0 \\ 0 & \sqrt{2} & 0 \\ 0 & 0 & 0 \end{pmatrix}, \quad T_1 = \begin{pmatrix} 0 & 0 & 1 \\ 0 & 0 & 1 \\ 0 & 0 & 0 \end{pmatrix}. \quad \text{(A4)}$$

The resulting lattice is shown in Fig. 7(b). A new unit cell can be identified considering the connected lattice sites (u_n, c_{n+1}, d_n), which affirms that the CLS stays in one unit cell and the class of the CLS is $U = 1$ in this representation. The corresponding lattice is shown in Fig. 7(c), and the matrices V_2 and T_2 are given by

$$V_2 = \begin{pmatrix} -\sqrt{2} & 1 & 0 \\ 1 & 0 & 1 \\ 0 & 1 & \sqrt{2} \end{pmatrix}, \quad T_2 = \begin{pmatrix} 0 & 0 & 0 \\ 0 & 0 & 0 \\ 0 & 0 & 0 \end{pmatrix}. \quad \text{(A5)}$$

Identifying the CLS in the new lattice, an inverse transformation can be performed to obtain the CLS in the diamond chain, which matches with Danieli *et al.* [99]. Hence the class of CLS is not unique under a transformation.

A further transformation can be performed to represent the lattice into a Fano defect form with decoupled sites. For this, the matrix H_2 will be defined as $H_2 = -V_2 - T_2 e^{ik} - T_2^\dagger e^{-ik}$ for the lattice in Fig. 7(c). We obtain the transformation matrix U_2 here from the eigenvectors of the matrix H_2, which is given
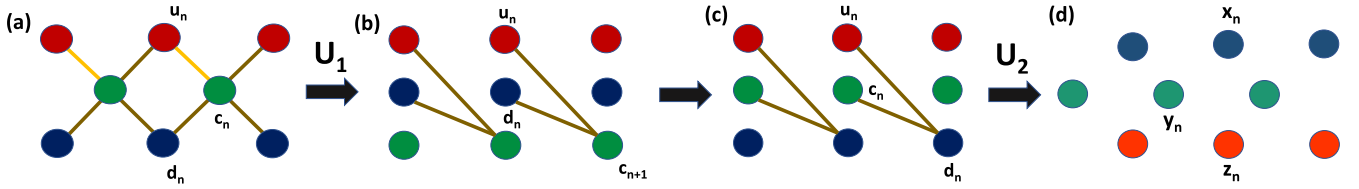
FIG. 7. Schematic representations of the transformation of the diamond chain into the new lattice with decoupled sites.

by

$$U_2 = \begin{pmatrix} \frac{3-2\sqrt{2}}{2\sqrt{6-4\sqrt{2}}} & \frac{2-\sqrt{2}}{2\sqrt{6-4\sqrt{2}}} & \frac{1}{2\sqrt{6-4\sqrt{2}}} \\ \frac{3+2\sqrt{2}}{2\sqrt{6+4\sqrt{2}}} & \frac{-2-\sqrt{2}}{2\sqrt{6+4\sqrt{2}}} & \frac{1}{2\sqrt{6+4\sqrt{2}}} \\ -\frac{1}{2} & -\frac{1}{\sqrt{2}} & \frac{1}{2} \end{pmatrix}. \tag{A6}$$

The transformed matrices $V_3 = U_2 V_2 U_2^\dagger$ and $T_3 = U_2 T_2 U_2^\dagger$ are

$$V_3 = \begin{pmatrix} 2 & 0 & 0 \\ 0 & -2 & 0 \\ 0 & 0 & 0 \end{pmatrix}, \quad T_3 = \begin{pmatrix} 0 & 0 & 0 \\ 0 & 0 & 0 \\ 0 & 0 & 0 \end{pmatrix}. \tag{A7}$$

The resulting lattice [see Fig. 7(d)] consists of three linear chains (x_n, y_n, z_n) without any hopping between sites. The isolated sites represent the flat band lattice in this representation, with the eigenstates strictly localized on only one site.

2. Transformation of ABF diamond chain with on-site potential

In the presence of on-site disorder, in addition to the intracell and intercell matrices, we introduce another matrix W_n given by

$$W_n = \begin{pmatrix} \zeta_n^u & 0 & 0 \\ 0 & \zeta_n^d & 0 \\ 0 & 0 & \zeta_n^c \end{pmatrix}, \tag{A8}$$

which is added in the general Hamiltonian: $H = W - V - T e^{ik} - T^\dagger e^{-ik}$. The transformation of the matrix W_n given by $U_1 W_n U_1^\dagger$ results in

$$(W_1)_n = \begin{pmatrix} \frac{\zeta_n^u}{4} + \frac{\zeta_n^d}{4} + \frac{\zeta_n^c}{2} & \frac{-\zeta_n^u}{4} + \frac{-\zeta_n^d}{4} + \frac{\zeta_n^c}{2} & \frac{\zeta_n^u}{2\sqrt{2}} - \frac{\zeta_n^d}{2\sqrt{2}} \\ \frac{-\zeta_n^u}{4} + \frac{-\zeta_n^d}{4} + \frac{\zeta_n^c}{2} & \frac{\zeta_n^u}{4} + \frac{\zeta_n^d}{4} + \frac{\zeta_n^c}{2} & \frac{-\zeta_n^u}{2\sqrt{2}} + \frac{\zeta_n^d}{2\sqrt{2}} \\ \frac{\zeta_n^u}{2\sqrt{2}} - \frac{\zeta_n^d}{2\sqrt{2}} & \frac{-\zeta_n^u}{2\sqrt{2}} + \frac{\zeta_n^d}{2\sqrt{2}} & \frac{\zeta_n^u}{2} + \frac{\zeta_n^d}{2} \end{pmatrix}, \tag{A9}$$

in addition to V_1 and T_1 for the transformed lattice. As before, rearranging the unit cell, new matrices incorporating the on-site contributions can be obtained as

$$V_{(W_2)_n} = \begin{pmatrix} \frac{\zeta_n^u}{4} + \frac{\zeta_n^d}{4} + \frac{\zeta_n^c}{2} & 0 & \frac{\zeta_n^u}{2\sqrt{2}} - \frac{\zeta_n^d}{2\sqrt{2}} \\ 0 & \frac{\zeta_{n+1}^u}{2} + \frac{\zeta_{n+1}^d}{2} & 0 \\ \frac{\zeta_n^u}{2\sqrt{2}} - \frac{\zeta_n^d}{2\sqrt{2}} & 0 & \frac{\zeta_n^u}{4} + \frac{\zeta_n^d}{4} + \frac{\zeta_n^c}{2} \end{pmatrix}, \tag{A10a}$$

$$T_{(W_2)_n} = \begin{pmatrix} 0 & 0 & 0 \\ \frac{\zeta_n^u}{2\sqrt{2}} - \frac{\zeta_n^d}{2\sqrt{2}} & 0 & -\frac{\zeta_n^u}{2\sqrt{2}} + \frac{\zeta_n^d}{2\sqrt{2}} \\ 0 & 0 & 0 \end{pmatrix}, \tag{A10b}$$

in addition to V_2 and T_2.

Similarly, we can obtain $V_{(W_3)_n} = U_2 V_{(W_2)_n} U_2^\dagger$ and $T_{(W_3)_n} = U_2 T_{(W_2)_n} U_2^\dagger$ in addition to V_3 and T_3 as

$$V_{(W_3)_n} = \begin{pmatrix} \zeta_1 & \zeta_2 & \zeta_3 \\ \zeta_2 & \zeta_1 & -\zeta_3 \\ \zeta_3 & -\zeta_3 & \zeta_4 \end{pmatrix}, \tag{A11}$$

$$T_{(W_3)_n} = \begin{pmatrix} \zeta_5 & -\zeta_5 & \zeta_6 \\ -\zeta_5 & \zeta_5 & -\zeta_6 \\ \zeta_6 & -\zeta_6 & -\frac{1}{2}\zeta_5 \end{pmatrix}, \tag{A12}$$

where $\zeta_1 = \frac{1}{8}(\zeta_n^u + \zeta_n^d + 4\zeta_n^c + \zeta_{n+1}^u + \zeta_{n+1}^d)$, $\zeta_2 = \frac{1}{8}(-\zeta_n^u - \zeta_n^d + 4\zeta_n^c - \zeta_{n+1}^u - \zeta_{n+1}^d)$, $\zeta_3 = \frac{1}{4\sqrt{2}}(\zeta_n^u + \zeta_n^d - \zeta_{n+1}^u - \zeta_{n+1}^d)$, $\zeta_4 = \frac{1}{4}(\zeta_n^u + \zeta_n^d + \zeta_{n+1}^u + \zeta_{n+1}^d)$, $\zeta_5 = \frac{1}{8}(-\zeta_{n+1}^u + \zeta_{n+1}^d)$, and $\zeta_6 = \frac{1}{4\sqrt{2}}(-\zeta_{n+1}^u + \zeta_{n+1}^d)$.

a. Symmetric case

Disorder on u and d sites. First, we consider the case with $\zeta_n^u = \zeta_n^d \neq 0$ and $\zeta_n^c = 0$.

Here the effects of on-site disorder incorporated through Eqs. (A11) and (A12) together with Eq. (A7) of the unperturbed lattice, result in matrices V_{S_1} and T_{S_1} [100] which represent the intracell and intercell hopping of the lattice:

$$V_{S_1} = \begin{pmatrix} \frac{1}{8}(2\zeta_n^u + 2\zeta_{n+1}^u) + 2 & \frac{1}{8}(-2\zeta_n^u - 2\zeta_{n+1}^u) & \frac{1}{4\sqrt{2}}(2\zeta_n^u - 2\zeta_{n+1}^u) \\ \frac{1}{8}(-2\zeta_n^u - 2\zeta_{n+1}^u) & \frac{1}{8}(2\zeta_n^u + 2\zeta_{n+1}^u) - 2 & \frac{1}{4\sqrt{2}}(-2\zeta_n^u + 2\zeta_{n+1}^u) \\ \frac{1}{4\sqrt{2}}(2\zeta_n^u - 2\zeta_{n+1}^u) & \frac{1}{4\sqrt{2}}(-2\zeta_n^u + 2\zeta_{n+1}^u) & \frac{1}{4}(2\zeta_n^u + 2\zeta_{n+1}^u) \end{pmatrix}, \quad T_{S_1} = \begin{pmatrix} 0 & 0 & 0 \\ 0 & 0 & 0 \\ 0 & 0 & 0 \end{pmatrix}. \tag{A13}$$

The corresponding lattice [see Fig. 8(a)] shows that the symmetric nature of the disorder decouples the unit cells of the system. The transformed lattice is a linear chain of uncoupled unit cells, implying that the states do not hybridize. At the same time, their probability amplitudes

may be rearranged along the sites to satisfy the lattice equation.

Disorder on c sites. We next consider another type of symmetric configuration where disorder is introduced only on the c sites, i.e., $\zeta_n^u = \zeta_n^d = 0$ and $\zeta_n^c \neq 0$. Here Eqs. (A11) and
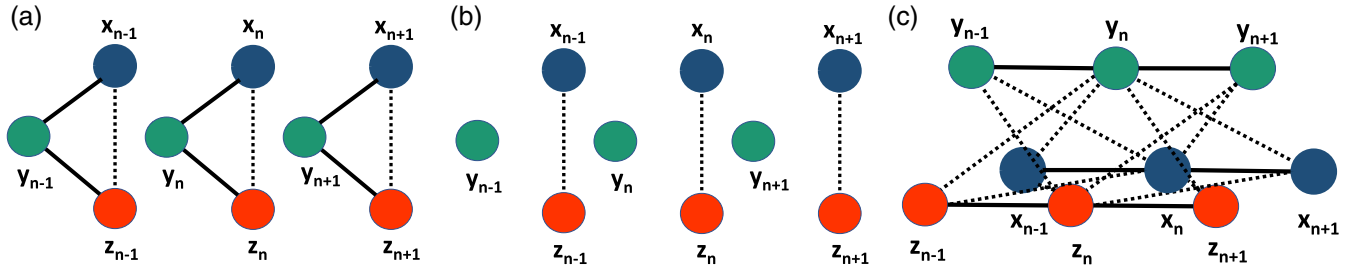
FIG. 8. Schematic representations of the new lattice with disorder in the symmetric case: (a) $\zeta_n^u = \zeta_n^d \neq 0$, $\zeta_n^c = 0$, (b) $\zeta_n^u = \zeta_n^d = 0$, $\zeta_n^c \neq 0$, and (c) the antisymmetric case: $\zeta_n^u = -\zeta_n^d \neq 0$, $\zeta_n^c = 0$

(A12) together with Eq. (A7) for the unperturbed lattice, give matrices V_{S_2} and T_{S_2}:

$$
V_{S_2} = \begin{pmatrix} \frac{\zeta_n^c}{2} + 2 & \frac{\zeta_n^c}{2} & 0 \\ \frac{\zeta_n^c}{2} & \frac{\zeta_n^c}{2} - 2 & 0 \\ 0 & 0 & 0 \end{pmatrix}, \quad T_{S_2} = \begin{pmatrix} 0 & 0 & 0 \\ 0 & 0 & 0 \\ 0 & 0 & 0 \end{pmatrix}.
$$

(A14)

As observed from Eq. (A14), there is no intercell hopping here. However, we find intracell hopping between two sites and an uncoupled site in a unit cell [see Fig. 8(b)].

b. Antisymmetric case

In the antisymmetric case, $\zeta_n^u = -\zeta_n^d$ while $\zeta_n^c = 0$. Then Eqs. (A11) and (A12) in addition to V_3 and T_3 [see Eq. (A7)] for the unperturbed lattice, give matrices V_A and T_A which represent the intracell and intercell hopping in the lattice:

$$
V_A = \begin{pmatrix} 2 & 0 & 0 \\ 0 & -2 & 0 \\ 0 & 0 & 0 \end{pmatrix}, \quad T_A = \begin{pmatrix} \frac{-\zeta_{n+1}^u}{4} & \frac{\zeta_{n+1}^u}{4} & \frac{-\zeta_{n+1}^u}{2\sqrt{2}} \\ \frac{\zeta_{n+1}^u}{4} & \frac{-\zeta_{n+1}^u}{4} & \frac{\zeta_{n+1}^u}{2\sqrt{2}} \\ \frac{\zeta_{n+1}^u}{2\sqrt{2}} & \frac{-\zeta_{n+1}^u}{2\sqrt{2}} & \frac{\zeta_{n+1}^u}{2} \end{pmatrix}.
$$

(A15)

The lattice corresponding to it is shown in Fig. 8(c). We observe that the resulting lattice is a three-leg cross-stitch chain. The intercell hopping in the lattice results in the nonexistence of the CLSs, unlike the symmetric case. We observe from the transformed lattice that the potential in the antisymmetric case leads to coupling between the adjacent unit cells. Still, the sites in a single unit cell remain decoupled. At low potential strengths, in the absence of intra-cell coupling, the nearest-neighbor (NN) intercell coupling leads to the multifractal nature of the eigenstates. As the strength of λ increases, the stronger coupling leads to Anderson localization.

APPENDIX B: COMPLEMENTARY QUANTITIES

In this section, we point out the usefulness of discussing several complementary quantities when the Aubry-André potential is applied in an antisymmetric manner. We also analyze the effect of the antisymmetric application of the uniform disorder through various measures.

1. AA disorder

The normalized participation ratio (PR) [101] is closely related to the inverse participation ratio and is given by

$$
P_k = \left[N \sum_{n=1}^{\frac{N}{3}} \sum_{\alpha=u,c,d} |\psi_k(\alpha_n)|^4 \right]^{-1}.
$$

(B1)

It vanishes for a perfectly localized eigenstate and goes to unity for a perfectly delocalized eigenstate. In Fig. 9(a), we have plotted the IPR, and the PR averaged over all the eigenstates in the inner part (shown with solid line) and the outer part (shown with dashed line) of the fractal mobility edge $\lambda = 4/|E|$ [77], with increasing strength of λ. These two quantities together help in the identification of the transition region. The transition from the extended $(0 < \mathrm{PR} < 1)$ to the Anderson localized regime lies around $\lambda \simeq 1.5$. This is because, in the zero disorder limit, the gaps between the flat bands are precisely of size 2, and thus a disorder strength of around 1.5–2 allows an interband hybridization.

Another measure that provides an understanding of the extent of localization in a system is the single-particle von Neumann entanglement entropy [102]. The von Neumann entropy associated with site α of the nth unit cell in the kth eigenstate is given by [103]

$$
\begin{aligned}
S_k^{\alpha_n} = & - |\psi_k(\alpha_n))|^2 \log_2(|\psi_k(\alpha_n)|^2) \\
& - (1 - |\psi_k(\alpha_n)|^2) \log_2(1 - |\psi_k(\alpha_n)|^2).
\end{aligned}
$$

(B2)

For a delocalized eigenstate $|\psi_k(\alpha_n)|^2 = 1/N$ and hence $S_k^{\alpha_n} \approx \frac{1}{N} \log_2 N + \frac{1}{N}$ for large values of N whereas for an eigenstate localized on a single-site $S_k^{\alpha_n} = 0$. The contributions from all sites for a particular eigenstate are given by $S_k = \sum_{n,\alpha} S_k^{\alpha_n}$. Thus the average von Neumann entropy over all the eigenstates is defined as

$$
S^{\mathrm{sp}} = \frac{\sum_{k=1}^N S_k}{N}.
$$

(B3)

For large values of N, $S^{\mathrm{sp}} \approx (\log_2 N + 1)$ in the delocalized phase whereas $S^{\mathrm{sp}} \approx 0$ in an extremely (single-site) localized phase. Figure 9(b) shows the single-particle entanglement entropy averaged over all the eigenstates in the inner part (shown with solid line) and the outer part (shown with dashed line) of the fractal mobility edge $\lambda = 4/|E|$ [77], with increasing strength of λ for various system sizes. Here, we observe a system size dependence in S^{sp} for the states in the inner region with its magnitude being marginally less than its maximum
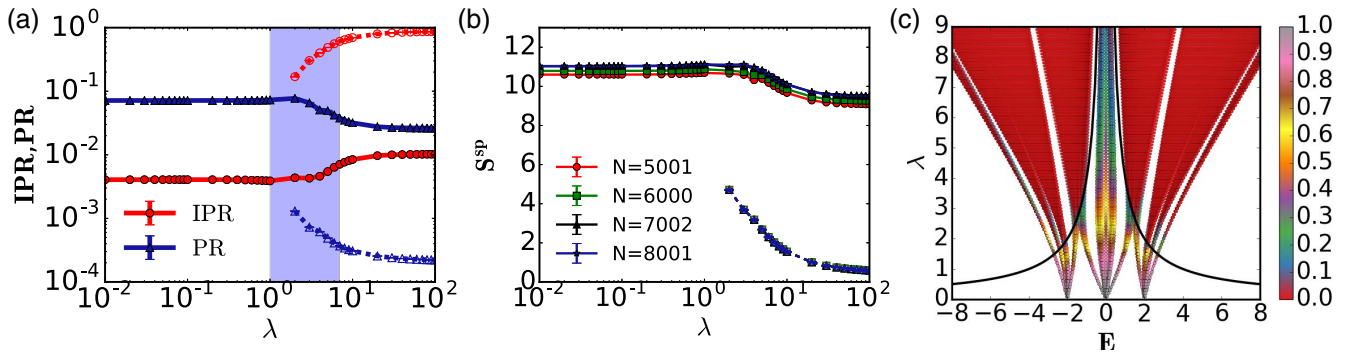
FIG. 9. In the antisymmetric case, (a) IPR and PR averaged of all the single-particle eigenstates separated by the fractal mobility edge $\lambda = 4/|E|$ (solid lines with filled symbols for states in the inner region and dashed lines with open symbols for states in the outer region) with increasing strength of AA potential λ for $N = 6000$ averaged over 50 values of θ_p. The shaded region signifies the transition of the eigenstates from extended to Anderson localization. (b) Single-particle von Neumann entropy S^{sp} averaged over the eigenstates separated by the fractal mobility edge (solid lines with solid symbols for states in the inner region and dashed lines with open symbols for states in the outer region) with increasing strength of AA potential λ for various system sizes. Averaging has been done over 50 values of θ_p for all cases. (c) The spectrum of the diamond lattice, where the color denotes the value of fidelity F with respect to eigenstates at $\lambda = 0.1$. Here the system size considered is $N = 6000$. The black solid line in panel (c) shows the transition between multifractal and localized states, conjectured in a recent preprint [77] using an analogy to the extended Harper problem (see Sec. V for more details).

value, which is a sign of the extended nature of the eigenstates. S^{sp} is largely system-size independent with its magnitude approaching $O(10^{-1})$, for the states outside the fractal mobility edge indicating Anderson localization.

We have also plotted the fidelity or overlap between the eigenstates, which helps distinguish extended and localized regions in the spectrum. Fidelity between the kth eigenstates corresponding to two values of λ is given by

$$F_{12}^k = |\langle \psi_k(\lambda_1) \mid \psi_k(\lambda_2)\rangle|^2. \tag{B4}$$

By choosing the first parameter λ_1 as the reference point, the second parameter λ_2 is varied in Fig. 9(c). We have previously shown that all the states below $\lambda \approx 1.5$ have multifractal nature. We observe that for larger λ the magnitude of fidelity is close to zero for all the states (except the central band) indicating localization. For the central band, for all values of λ, the fidelity $0 < F < 1$. This indicates that though the states are multifractal in the central band, the amplitude distribution on the lattice sites does not remain fixed with increasing strength of the potential λ.

Scaling analysis

The scaling analysis of the distribution of the IPR logarithm $P(\ln I_2)$ at the critical point shows invariance of shape or width with increasing system size N [104]. After shifting the curves along the x axis, they all lie on top of each other, forming a scale-invariant IPR distribution. We utilize this measure and analyze all the nonergodic extended states at low $-\lambda = 0.01$ [see Fig. 10(a)] and those separated by the fractal mobility edge [77] $\lambda_c = \frac{4}{|E|}$ at high $-\lambda = 10$ [see Fig. 10(b)] and observe that the distributions of IPR are indeed scale invariant. However, for the states outside the fractality edge at a higher disorder strength (like $\lambda = 10$), we observe that the distribution is independent of N, confirming that the states are localized [see Fig. 10(c)].

We also perform a multifractal analysis of the wave functions using the box-counting method. For the AAH model,

it was observed that the wave functions exhibit multifractal behavior extending to all length scales at the critical point. For localized states, multifractal features are observed up to the localization length and for extended states they are observed up to the correlation length [105]. We analyze the multifractal properties here by coarse-graining the system into boxes of length l. Given a normalized wave function $|\psi_k\rangle = \sum_{i=1}^{N} \psi_k(i)|i\rangle$ defined over a lattice of size N, we divide the lattice into N/l segments of length l [106]:

$$\chi_j(q) = \sum_{p=1}^{N/l} \left[\sum_{i=(p-1)l+1}^{pl} |\psi_k(i)|^2 \right]^q. \tag{B5}$$

The average is then considered over the total number of states in the central band (CB) j_{CB}:

$$\chi(q)_{CB} = \frac{1}{j_{CB}} \sum_{j}^{j_{CB}} \chi_j(q), \tag{B6}$$

and the total number of states of the sidebands (SB) j_{SB}:

$$\chi(q)_{SB} = \frac{1}{j_{SB}} \sum_{j}^{j_{SB}} \chi_j(q). \tag{B7}$$

Multifractality is characterized by a power-law behavior of $\chi(q) \sim (l/L)^{\tau(q)}$ with the exponent $\tau(q)$ determining the multifractal dimension $D_q = \tau(q)/(q-1)$ where $q = 2$ gives $\tau(2) = D_2$. In Figs. 10(d)–10(f), we display the change of $\ln \chi$ as a function of $\ln l$ for different system sizes. In the critical regime, it is found that $\ln \chi$ is a linear function of $\ln l$ described by a series of parallel lines for different N with the same slope D_2. We observe this behavior for the all states at low $-\lambda = 0.01$ [see Fig. 10(d)] with $D_2 = 0.63 \pm 0.005$ indicating that they are indeed nonergodic extended. The same is observed at high $-\lambda = 10$, for the states comprising the inner band of the fractal mobility edge [77] $\lambda_c = 4/|E|$ with $D_2 = 0.61 \pm 0.005$ [see Fig. 10(e)]. In the localized region, for lengths less than the localization length $l < l_c$, $\ln \chi$ is a
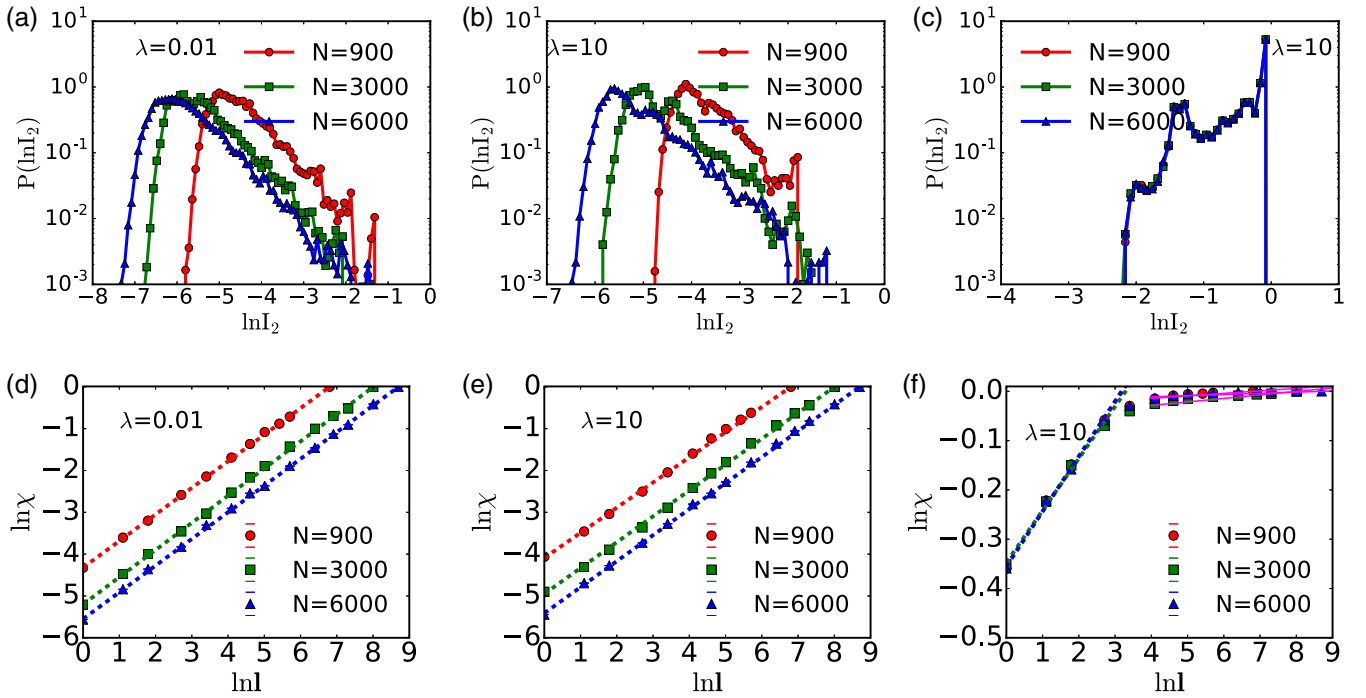
FIG. 10. In the antisymmetric case, distribution of $P(\ln I_2)$ for different system sizes computed using (a) all the eigenstates at $\lambda = 0.01$ (b) multifractal states comprising the inner region of the fractal mobility edge $\lambda = 4/|E|$, conjectured in Ref. [77] at $\lambda = 10$ and (c) localized states that exist in the outer region of the fractal mobility edge at $\lambda = 10$. The change of $\ln \chi$ as a function of $\ln l$ for different system sizes computed using (d) all the eigenstates at $\lambda = 0.01$ (e) multifractal eigenstates comprising the inner region of the fractal mobility edge $\lambda = 4/|E|$, at $\lambda = 10$ and (f) localized states that exists in the outer region of the fractal mobility edge at $\lambda = 10$.

linear function of $\ln l$, which completely superposes together for different N with an identical slope of D_2—so one might naively conclude that the system exhibits multifractal behavior. However for $l > l_c$ the slopes decrease to 0. The same can be observed for all the states outside the fractal mobility edge at high $-\lambda$ [see Fig. 10(f)] with $D_2 \approx 0.11$ (fitted with the dotted curves) for $l < l_c$ while the slopes decrease to 0 (fitted with the magenta lines) for $l > l_c$, thus showing that in fact these states are localized.

2. Uniform uncorrelated random disorder

We have also analyzed the application of the uniform uncorrelated random disorder in an antisymmetric manner. Here Δ is the disorder strength. We observe from Fig. 11(a) that the average gap ratio r [107,108] remains around the Poisson value (≈ 0.39) at all strengths of the disorder. Further from the energy-resolved IPR study [see Fig. 11(b)], it can be observed that all the eigenstates exhibit low IPR below $\Delta \approx 2$. The presence of a mobility edge is also observed here. Dividing Eq. (24) by Δ, we get

$$\frac{E}{\Delta}[E^2 - 4]c_n = w_n \frac{\Delta E}{2} c_n - t_n c_{n+1} - t_{n-1} c_{n-1}, \quad \text{(B8)}$$

where $t_n = \zeta_n/\Delta$ are i.i.d. random numbers, homogeneously distributed in a unit interval $|t_n| < 1$, while $w_n = 4\zeta_n^2/\Delta^2$ are i.i.d. random numbers, whose distribution $P(w_n) \sim \theta(1 - w_n)/(2\sqrt{w_n})$ is singular but integrable due to the cut tail for $|w_n| > 1$. From this, one can estimate the finite-size mobility edge as the line where the localization length $\xi(E)$,

determining the eigenstate exponential decay

$$|\psi_E(r)| \sim e^{-|r-r_E|/\xi_E} \quad \text{(B9)}$$

with respect to the random energy-dependent maximum r_E, is of the order of the system size $\xi(E) \simeq N$.

The expression for $\xi(E)$ can be estimated as (see, e.g., Ref. [109])

$$\xi_E \simeq F\left(\frac{E t_{typ}}{w_{typ}^2}\right) \frac{t_{typ}^2}{w_{typ}^2}, \quad \text{(B10)}$$

where a smooth function $F(x) \simeq O(N^0)$ [110] can be replaced by a constant as it changes by 10 % from $x = 0$ to $x = \infty$ and the typical value w_{typ} (t_{typ}) of the on-site disorder w_n (hopping t_n) is given by the typical value of the distributions of $P(\ln w_n)$ $(P(\ln t_n))$. In our case,

$$w_{typ} = e^{\langle \ln w_n \rangle} = e^{-2}, \quad t_{typ} = e^{\langle \ln t_n \rangle} = e^{-1}, \quad \text{(B11)}$$

i.e.,

$$\xi_E(N) \simeq \left(\frac{2e}{\Delta|E|}\right)^2 F. \quad \text{(B12)}$$

Thus, from $\xi_E \simeq N$, we get

$$\Delta_c(E) = \frac{2e}{E} \sqrt{\frac{F}{N}}. \quad \text{(B13)}$$

This demonstrates that the mobility edge, shown in Fig. 11(b) for $N = 6000$ and $F = 6000$ is a finite-size effect. However, on the other hand, it also shows why the state at exactly zero energy $E = 0$ (which exists for odd N) will not localize. The
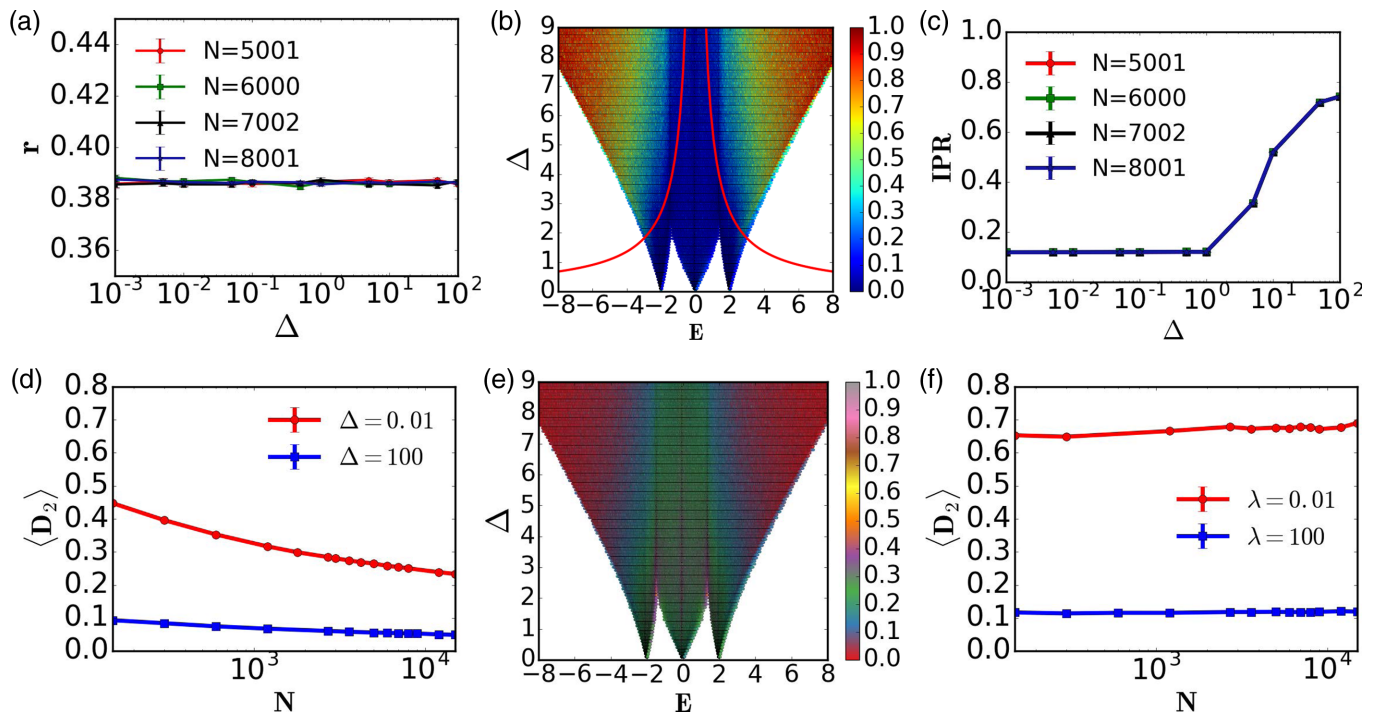
FIG. 11. In the antisymmetric case (a) gap ratio r [107,108] and (c) IPR averaged over all the eigenstates for uniform uncorrelated random disorder with increasing strength Δ for various system sizes. The averaging has been done over 50 values of θ_p. The spectrum of system size $N = 6000$ with increasing strength of disorder Δ, where the color denotes the value of (b) IPR and (e) fractal dimension D_2 for all the single-particle eigenstates. D_2 averaged over all the eigenstates with increasing system size when applied disorder is (d) uniform uncorrelated random disorder and (f) quasiperiodic AA disorder.

latter is related to the conserved chiral symmetry in the system, where the low energy states may keep their delocalized nature even in the 1d chiral Anderson model. In any case this regime deserves further detailed investigations in future works.

From the IPR averaged over all the eigenstates [see Fig. 11(c)], we observe that it is system size-independent, indicating localization. Thus while the averaged gap ratio and IPR suggest localization for the entire disorder range, the same is not observed from the energy-resolved IPR. The spectrum resolved fractal dimension D_2 is plotted in Fig. 11(e). While the eigenstates below $\Delta \approx 2$ and those belonging to the central band remain multifractal with $D_2 \approx 0.2$, they are less extended when the applied perturbation is AA ($D_2 \approx 0.6$).

Thus we infer that the localization characteristics of the eigenstates in the low-disorder regime depends on the nature of the applied potential. On the other hand, when the strength of the disorder is sufficient, the different bands hybridize, conventional Anderson localization takes over, and the details of the form of the disorder are not important. Figure 11(d) shows D_2 averaged over all the eigenstates when the uniform disorder is applied. The magnitude of D_2 decreases both in the low and high disorder regime with increasing system size, indicating a steady decline in the fraction of states exhibiting multifractality. In contrast, the fraction of states exhibiting the multifractal behavior remains robust for the AA potential Fig. 11(f). This suggests that the specific form of the AA potential has an important role in ensuring multifractality.

[1] S. A. Parameswaran, R. Roy, and S. L. Sondhi, Fractional quantum Hall physics in topological flat bands, C. R. Phys. **14**, 816 (2013), topological insulators / Isolants topologiques.

[2] E. J. Bergholtz and Z. Liu, Topological flat band models and fractional Chern insulators, Int. J. Mod. Phys. B **27**, 1330017 (2013).

[3] O. Derzhko, J. Richter, and M. Maksymenko, Strongly correlated flat-band systems: The route from Heisenberg spins to Hubbard electrons, Int. J. Mod. Phys. B **29**, 1530007 (2015).

[4] S. Flach, D. Leykam, J. D. Bodyfelt, P. Matthies, and A. S. Desyatnikov, Detangling flat bands into Fano lattices, Europhys. Lett. **105**, 30001 (2014).

[5] D. Leykam, A. Andreanov, and S. Flach, Artificial flat band systems: from lattice models to experiments, Adv. Phys.: X **3**, 1473052 (2018).

[6] W. Maimaiti, A. Andreanov, H. C. Park, O. Gendelman, and S. Flach, Compact localized states and flat-band generators in one dimension, Phys. Rev. B **95**, 115135 (2017).

[7] P. Sathe, F. Harper, and R. Roy, Compactly supported Wannier functions and strictly local projectors, J. Phys. A: Math. Theor. **54**, 335302 (2021).

[8] J. Vidal, B. Douçot, R. Mosseri, and P. Butaud, Interaction Induced Delocalization for Two Particles in a Periodic Potential, Phys. Rev. Lett. **85**, 3906 (2000).

[9] B. Douçot and J. Vidal, Pairing of Cooper Pairs in a Fully Frustrated Josephson-Junction Chain, Phys. Rev. Lett. **88**, 227005 (2002).

[10] S. Mukherjee, M. Di Liberto, P. Öhberg, R. R. Thomson, and N. Goldman, Experimental Observation of Aharonov-Bohm Cages in Photonic Lattices, Phys. Rev. Lett. **121**, 075502 (2018).

[11] J. D. Bodyfelt, D. Leykam, C. Danieli, X. Yu, and S. Flach, Flatbands under Correlated Perturbations, Phys. Rev. Lett. **113**, 236403 (2014).

[12] M. Tovmasyan, S. Peotta, L. Liang, P. Törmä, and S. D. Huber, Preformed pairs in flat Bloch bands, Phys. Rev. B **98**, 134513 (2018).

[13] C. Gneiting, Z. Li, and F. Nori, Lifetime of flatband states, Phys. Rev. B **98**, 134203 (2018).

[14] J. Vidal, R. Mosseri, and B. Douçot, Aharonov-Bohm Cages in Two-Dimensional Structures, Phys. Rev. Lett. **81**, 5888 (1998).

[15] J. Vidal, P. Butaud, B. Douçot, and R. Mosseri, Disorder and interactions in Aharonov-Bohm cages, Phys. Rev. B **64**, 155306 (2001).

[16] C. Naud, G. Faini, and D. Mailly, Aharonov-Bohm Cages in 2D Normal Metal Networks, Phys. Rev. Lett. **86**, 5104 (2001).

[17] A. R. Kolovsky, A. Ramachandran, and S. Flach, Topological flat Wannier-Stark bands, Phys. Rev. B **97**, 045120 (2018).

[18] C. Wu, D. Bergman, L. Balents, and S. Das Sarma, Flat Bands and Wigner Crystallization in the Honeycomb Optical Lattice, Phys. Rev. Lett. **99**, 070401 (2007).

[19] T. Jacqmin, I. Carusotto, I. Sagnes, M. Abbarchi, D. D. Solnyshkov, G. Malpuech, E. Galopin, A. Lemaître, J. Bloch, and A. Amo, Direct Observation of Dirac Cones and a Flatband in a Honeycomb Lattice for Polaritons, Phys. Rev. Lett. **112**, 116402 (2014).

[20] N. Masumoto, N. Y. Kim, T. Byrnes, K. Kusudo, A. Löffler, S. Höfling, A. Forchel, and Y. Yamamoto, Exciton–polariton condensates with flat bands in a two-dimensional kagome lattice, New J. Phys. **14**, 065002 (2012).

[21] G.-W. Chern, C.-C. Chien, and M. Di Ventra, Dynamically generated flat-band phases in optical kagome lattices, Phys. Rev. A **90**, 013609 (2014).

[22] G.-B. Jo, J. Guzman, C. K. Thomas, P. Hosur, A. Vishwanath, and D. M. Stamper-Kurn, Ultracold Atoms in a Tunable Optical Kagome Lattice, Phys. Rev. Lett. **108**, 045305 (2012).

[23] M. Trescher and E. J. Bergholtz, Flat bands with higher Chern number in pyrochlore slabs, Phys. Rev. B **86**, 241111(R) (2012).

[24] T. Mizoguchi and M. Udagawa, Flat-band engineering in tight-binding models: Beyond the nearest-neighbor hopping, Phys. Rev. B **99**, 235118 (2019).

[25] A. Mielke, Ferromagnetism in Single-Band Hubbard Models with a Partially Flat Band, Phys. Rev. Lett. **82**, 4312 (1999).

[26] H. Tasaki, From Nagaoka's Ferromagnetism to Flat-Band Ferromagnetism and Beyond: An Introduction to Ferromagnetism in the Hubbard Model, Prog. Theor. Phys. **99**, 489 (1998).

[27] D. Guzmán-Silva, C. Mejía-Cortés, M. A. Bandres, M. C. Rechtsman, S. Weimann, S. Nolte, M. Segev, A. Szameit, and R. A. Vicencio, Experimental observation of bulk and edge transport in photonic lieb lattices, New J. Phys. **16**, 063061 (2014).

[28] S. Mukherjee, A. Spracklen, D. Choudhury, N. Goldman, P. Öhberg, E. Andersson, and R. R. Thomson, Observation of a Localized Flat-Band State in a Photonic Lieb Lattice, Phys. Rev. Lett. **114**, 245504 (2015).

[29] Y. Zhang and C. Zhang, Bose-Einstein condensates in spin-orbit-coupled optical lattices: Flat bands and superfluidity, Phys. Rev. A **87**, 023611 (2013).

[30] E. Abrahams, P. W. Anderson, D. C. Licciardello, and T. V. Ramakrishnan, Scaling Theory of Localization: Absence of Quantum Diffusion in Two Dimensions, Phys. Rev. Lett. **42**, 673 (1979).

[31] F. Evers and A. D. Mirlin, Anderson transitions, Rev. Mod. Phys. **80**, 1355 (2008).

[32] P. W. Anderson, Absence of diffusion in certain random lattices, Phys. Rev. **109**, 1492 (1958).

[33] P. A. Lee and T. V. Ramakrishnan, Disordered electronic systems, Rev. Mod. Phys. **57**, 287 (1985).

[34] N. Roy, A. Ramachandran, and A. Sharma, Interplay of disorder and interactions in a flat-band supporting diamond chain, Phys. Rev. Res. **2**, 043395 (2020).

[35] S. Aubry and G. André, Analyticity breaking and Anderson localization in incommensurate lattices, Ann. Isr. Phys. Soc. **3**, 18 (1980).

[36] M. Modugno, Exponential localization in one-dimensional quasi-periodic optical lattices, New J. Phys. **11**, 033023 (2009).

[37] J. T. Chalker, T. S. Pickles, and P. Shukla, Anderson localization in tight-binding models with flat bands, Phys. Rev. B **82**, 104209 (2010).

[38] V. E. Kravtsov, I. M. Khaymovich, E. Cuevas, and M. Amini, A random matrix model with localization and ergodic transitions, New J. Phys. **17**, 122002 (2015).

[39] E. Bogomolny and M. Sieber, Eigenfunction distribution for the Rosenzweig-Porter model, Phys. Rev. E **98**, 032139 (2018).

[40] D. Facoetti, P. Vivo, and G. Biroli, From non-ergodic eigenvectors to local resolvent statistics and back: A random matrix perspective, Europhys. Lett. **115**, 47003 (2016).

[41] K. Truong and A. Ossipov, Eigenvectors under a generic perturbation: Non-perturbative results from the random matrix approach, Europhys. Lett. **116**, 37002 (2016).

[42] G. D. Tomasi, M. Amini, S. Bera, I. M. Khaymovich, and V. E. Kravtsov, Survival probability in Generalized Rosenzweig-Porter random matrix ensemble, SciPost Phys. **6**, 014 (2019).

[43] C. Monthus, Multifractality of eigenstates in the delocalized non-ergodic phase of some random matrix models: Wigner–Weisskopf approach, J. Phys. A: Math. Theor. **50**, 295101 (2017).

[44] M. Amini, Spread of wave packets in disordered hierarchical lattices, Europhys. Lett. **117**, 30003 (2017).

[45] V. E. Kravtsov, I. M. Khaymovich, B. L. Altshuler, and L. B. Ioffe, Localization transition on the random regular graph as an unstable tricritical point in a log-normal Rosenzweig-Porter random matrix ensemble, arXiv:2002.02979.

[46] I. M. Khaymovich, V. E. Kravtsov, B. L. Altshuler, and L. B. Ioffe, Fragile extended phases in the log-normal Rosenzweig-Porter model, Phys. Rev. Res. **2**, 043346 (2020).

[47] I. M. Khaymovich and V. E. Kravtsov, Dynamical phases in a "multifractal" Rosenzweig-Porter model, SciPost Phys. **11**, 045 (2021).

[48] N. Roy and A. Sharma, Study of counterintuitive transport properties in the Aubry-André-Harper model via entanglement entropy and persistent current, Phys. Rev. B **100**, 195143 (2019).

[49] X. Deng, S. Ray, S. Sinha, G. V. Shlyapnikov, and L. Santos, One-Dimensional Quasicrystals with Power-Law Hopping, Phys. Rev. Lett. **123**, 025301 (2019).

[50] D. Voliotis, Multifractality in aperiodic quantum spin chains, J. Phys. A: Math. Theor. **52**, 475001 (2019).

[51] M. Serbyn, Z. Papić, and D. A. Abanin, Thouless energy and multifractality across the many-body localization transition, Phys. Rev. B **96**, 104201 (2017).

[52] M. Pouranvari, Multifractality of the entanglement Hamiltonian eigenmodes, Phys. Rev. B **99**, 155121 (2019).

[53] Y. Wang, C. Cheng, X.-J. Liu, and D. Yu, Many-Body Critical Phase: Extended and Nonthermal, Phys. Rev. Lett. **126**, 080602 (2021).

[54] P. A. Nosov, I. M. Khaymovich, and V. E. Kravtsov, Correlation-induced localization, Phys. Rev. B **99**, 104203 (2019).

[55] P. Das and A. Sharma, Revisiting the phase transitions of the Dicke model, Phys. Rev. A **105**, 033716 (2022).

[56] Y. Takada, K. Ino, and M. Yamanaka, Statistics of spectra for critical quantum chaos in one-dimensional quasiperiodic systems, Phys. Rev. E **70**, 066203 (2004).

[57] K. Machida and M. Fujita, Quantum energy spectra and one-dimensional quasiperiodic systems, Phys. Rev. B **34**, 7367 (1986).

[58] D. J. Thouless, Bandwidths for a quasiperiodic tight-binding model, Phys. Rev. B **28**, 4272 (1983).

[59] C. Castellani and L. Peliti, Multifractal wavefunction at the localisation threshold, J. Phys. A: Math. Gen. **19**, L429 (1986).

[60] A. Ramachandran, A. Andreanov, and S. Flach, Chiral flat bands: Existence, engineering, and stability, Phys. Rev. B **96**, 161104(R) (2017).

[61] D. Leykam, J. D. Bodyfelt, A. S. Desyatnikov, and S. Flach, Localization of weakly disordered flat band states, Europhys. Lett. **90** (2017).

[62] C. Poli, H. Schomerus, M. Bellec, U. Kuhl, and F. Mortessagne, Partial chiral symmetry-breaking as a route to spectrally isolated topological defect states in two-dimensional artificial materials, 2D Mater. **4**, 025008 (2017).

[63] A. Štrkalj, E. V. H. Doggen, and C. Castelnovo, Coexistence of localization and transport in many-body two-dimensional Aubry-André models, arXiv:2204.05198 [Phys. Rev. B (to be published)].

[64] P. A. Nosov and I. M. Khaymovich, Robustness of delocalization to the inclusion of soft constraints in long-range random models, Phys. Rev. B **99**, 224208 (2019).

[65] W. Tang and I. M. Khaymovich, Non-ergodic delocalized phase with Poisson level statistics, Quantum **6**, 733 (2022).

[66] V. Motamarri, A. S. Gorsky, and I. M. Khaymovich, Localization and fractality in disordered Russian Doll model, arXiv:2112.05066 [SciPost Phys. (to be published)].

[67] A. G. Kutlin and I. M. Khaymovich, Emergent fractal phase in energy stratified random models, SciPost Phys. **11**, 101 (2021).

[68] A. Duthie, S. Roy, and D. E. Logan, Anomalous multifractality in quantum chains with strongly correlated disorder, Phys. Rev. B **106**, L020201 (2022).

[69] X. Cai, L.-J. Lang, S. Chen, and Y. Wang, Topological Superconductor to Anderson Localization Transition in One-Dimensional Incommensurate Lattices, Phys. Rev. Lett. **110**, 176403 (2013).

[70] W. DeGottardi, D. Sen, and S. Vishveshwara, Majorana Fermions in Superconducting 1D Systems Having Periodic, Quasiperiodic, and Disordered Potentials, Phys. Rev. Lett. **110**, 146404 (2013).

[71] J. Wang, X.-J. Liu, G. Xianlong, and H. Hu, Phase diagram of a non-Abelian Aubry-André-Harper model with *p*-wave superfluidity, Phys. Rev. B **93**, 104504 (2016).

[72] C. Danieli, J. D. Bodyfelt, and S. Flach, Flat-band engineering of mobility edges, Phys. Rev. B **91**, 235134 (2015).

[73] Here we note that the choice of periodic boundary conditions is not very important, as the quasiperiodic potential anyway has a jump at the boundary. Unlike some other models, we do not put the rational approximants *M*/*N* of *b* by taking certain system sizes *N* from the above approximations.

[74] J. K. Asboth, L. Oroszlany, and A. Palyi, *A Short Course on Topological Insulators* (Springer, Switzerland, 2016), Vol. 919.

[75] S. Ryu, A. P. Schnyder, A. Furusaki, and A. W. W. Ludwig, Topological insulators and superconductors: Tenfold way and dimensional hierarchy, New J. Phys. **12**, 065010 (2010).

[76] A. W. W. Ludwig, Topological phases: Classification of topological insulators and superconductors of non-interacting fermions, and beyond, Phys. Scr. **T168**, 014001 (2016).

[77] S. Lee, A. Andreanov, and S. Flach, Critical-to-insulator transitions and fractality edges in perturbed flatbands, arXiv:2208.11930.

[78] J. Lindinger, A. Buchleitner, and A. Rodríguez, Many-Body Multifractality throughout Bosonic Superfluid and Mott Insulator Phases, Phys. Rev. Lett. **122**, 106603 (2019).

[79] N. Macé, F. Alet, and N. Laflorencie, Multifractal Scalings Across the Many-Body Localization Transition, Phys. Rev. Lett. **123**, 180601 (2019).

[80] A. D. Mirlin and F. Evers, Multifractality and critical fluctuations at the Anderson transition, Phys. Rev. B **62**, 7920 (2000).

[81] A. Bäcker, M. Haque, and I. M. Khaymovich, Multifractal dimensions for random matrices, chaotic quantum maps, and many-body systems, Phys. Rev. E **100**, 032117 (2019).

[82] N. Meenakshisundaram and A. Lakshminarayan, Multifractal eigenstates of quantum chaos and the Thue-Morse sequence, Phys. Rev. E **71**, 065303(R) (2005).

[83] S. N. Evangelou and J.-L. Pichard, Critical Quantum Chaos and the One-Dimensional Harper Model, Phys. Rev. Lett. **84**, 1643 (2000).

[84] M. Janssen, Multifractal analysis of broadly-distributed observables at criticality, Int. J. Mod. Phys. B **08**, 943 (1994).

[85] C. P. Chen, M. Szyniszewski, and H. Schomerus, Many-body localization of zero modes, Phys. Rev. Res. **2**, 023118 (2020).

[86] Y.-J. Wu and J. Hou, Symmetry-protected localized states at defects in non-Hermitian systems, Phys. Rev. A **99**, 062107 (2019).

[87] N. Leumer, M. Marganska, B. Muralidharan, and M. Grifoni, Exact eigenvectors and eigenvalues of the finite Kitaev chain and its topological properties, J. Phys.: Condens. Matter **32**, 445502 (2020).

[88] V. Z. Cerovski, Bond-disordered Anderson model on a two-dimensional square lattice: Chiral symmetry and

restoration of one-parameter scaling, Phys. Rev. B **62**, 12775 (2000).

[89] A. M. García-García and E. Cuevas, Anderson transition in systems with chiral symmetry, Phys. Rev. B **74**, 113101 (2006).

[90] C. Mudry, P. W. Brouwer, and A. Furusaki, Crossover from the chiral to the standard universality classes in the conductance of a quantum wire with random hopping only, Phys. Rev. B **62**, 8249 (2000).

[91] F. J. Dyson, The dynamics of a disordered linear chain, Phys. Rev. **92**, 1331 (1953).

[92] A. Avila, S. Jitomirskaya, and C. A. Marx, Spectral theory of extended Harpers model and a question by Erdös and Szekeres, Invent. Math. **210**, 283 (2017).

[93] The factor of 2 (also mentioned in Ref. [77]) with respect to the extended Harper model comes from the two times larger level spacing given by the derivative of the potential.

[94] J. H. Han, D. J. Thouless, H. Hiramoto, and M. Kohmoto, Critical and bicritical properties of Harper's equation with next-nearest-neighbor coupling, Phys. Rev. B **50**, 11365 (1994).

[95] A. Rodriguez, L. J. Vasquez, K. Slevin, and R. A. Römer, Critical Parameters from a Generalized Multifractal Analysis at the Anderson Transition, Phys. Rev. Lett. **105**, 046403 (2010).

[96] I. Chang, K. Ikezawa, and M. Kohmoto, Multifractal properties of the wave functions of the square-lattice tight-binding model with next-nearest-neighbor hopping in a magnetic field, Phys. Rev. B **55**, 12971 (1997).

[97] F. Liu, S. Ghosh, and Y. D. Chong, Localization and adiabatic pumping in a generalized Aubry-André-Harper model, Phys. Rev. B **91**, 014108 (2015).

[98] Y. E. Kraus and O. Zilberberg, Topological Equivalence between the Fibonacci Quasicrystal and the Harper Model, Phys. Rev. Lett. **109**, 116404 (2012).

[99] C. Danieli, A. Andreanov, T. Mithun, and S. Flach, Nonlinear caging in all-band-flat lattices, Phys. Rev. B **104**, 085131 (2021).

[100] Here and further the subscripts S and A correspond to the symmetric and antisymmetric cases.

[101] X. Li, X. Li, and S. Das Sarma, Mobility edges in one-dimensional bichromatic incommensurate potentials, Phys. Rev. B **96**, 085119 (2017).

[102] L. Gong and P. Tong, Fidelity, fidelity susceptibility, and von Neumann entropy to characterize the phase diagram of an extended Harper model, Phys. Rev. B **78**, 115114 (2008).

[103] X. Jia, A. R. Subramaniam, I. A. Gruzberg, and S. Chakravarty, Entanglement entropy and multifractality at localization transitions, Phys. Rev. B **77**, 014208 (2008).

[104] F. Evers and A. D. Mirlin, Fluctuations of the Inverse Participation Ratio at the Anderson Transition, Phys. Rev. Lett. **84**, 3690 (2000).

[105] A. P. Siebesma and L. Pietronero, Multifractal properties of wave functions for one-dimensional systems with an incommensurate potential, Europhys. Lett. **4**, 597 (1987).

[106] Y. Wang, Y. Wang, and S. Chen, Spectral statistics, finite-size scaling and multifractal analysis of quasiperiodic chain with p-wave pairing, Eur. Phys. J. B **89**, 254 (2016).

[107] V. Oganesyan and D. A. Huse, Localization of interacting fermions at high temperature, Phys. Rev. B **75**, 155111 (2007).

[108] Y. Y. Atas, E. Bogomolny, O. Giraud, and G. Roux, Distribution of the Ratio of Consecutive Level Spacings in Random Matrix Ensembles, Phys. Rev. Lett. **110**, 084101 (2013).

[109] L. Sanchez-Palencia, D. Clément, P. Lugan, P. Bouyer, G. V. Shlyapnikov, and A. Aspect, Anderson Localization of Expanding Bose-Einstein Condensates in Random Potentials, Phys. Rev. Lett. **98**, 210401 (2007).

[110] In a standard Anderson model $F \simeq 100$, but we consider it as a constant fitting parameter.